

THERAPEUTIC POTENTIAL OF THE ANTI-FIBROTIC DRUG
SUBERANILOHYDROXAMIC ACID (SAHA) IN CANINE CORNEAL FIBROSIS

A Thesis presented to the Faculty of the Graduate School
University of Missouri-Columbia

In Partial Fulfillment
Of the Requirements for the Degree
Master of Science

By
KRISTINA GRONKIEWICZ
Dr. Elizabeth A. Giuliano, Thesis Supervisor

MAY 2016

The undersigned, appointed by the dean of the Graduate School, have examined the thesis entitled

**THERAPEUTIC POTENTIAL OF THE ANTI-FIBROTIC DRUG
SUBERANILOHYDROXAMIC ACID (SAHA) IN CANINE CORNEAL
FIBROSIS**

Presented by Kristina Gronkiewicz,

A candidate for the degree of Master of Science,

And hereby certify that, in their opinion, it is worthy of acceptance..

Dr. Elizabeth Giuliano

Dr. Jacqueline Pearce

Dr. Cecil Moore

Dr. Rajiv Mohan

Dr. Mahesh Thakkar

DEDICATION

I dedicate my thesis to my loving and supportive parents, Theresa and Nicholas Gronkiewicz, for their words of encouragement and also Theresa's outstanding editorial capabilities. Thank you so much for standing by my side as I achieved my childhood dreams of becoming a veterinarian. You are both very special to me and I am extremely proud to be your daughter.

ACKNOWLEDGEMENTS

The author would like to thank the following individuals:

Dr. Elizabeth A. Giuliano, for her continuous support, patience, motivation and knowledge which allowed for the success of this extensive research project and my clinical ophthalmology residency program.

Drs. Rajiv M. Mohan and Ajay Sharma, for their assistance in experimental design, patience and encouragement during these studies. Your insightful comments and questions were extremely helpful and pushed me to widen the scope of my research.

Drs. Cecil P. Moore and Jacqueline Pearce for their mentorship and encouragement during my clinical ophthalmology residency program. Without your support during clinics, I would not have been able to conduct this research.

Dr. Filiz Bunyak, for her ingenuity in transmission electron microscopy image processing and analysis.

Drs. Kei Kuroki and Leandro Teixeira, for their assistance in histological and immunohistochemical analysis.

Dr. Richard D. Madsen, for statistical assistance.

Ms. Jessica Kitchell and Melanie Kunkel and Mr. Chuck W. Hamm, for their technical assistance

Supported by grants from the American College of Veterinary Ophthalmologists - Vision for Animals, University of Missouri, Phi Zeta Society and the University of Missouri, Research Council and also funds from the Ruth M. Kraeuchi Ophthalmology Endowment.

TABLE OF CONTENTS

ACKNOWLEDGEMENTS	ii
LIST OF TABLES	vi
LIST OF FIGURES	vii
LIST OF ABBREVIATIONS.....	ix
ABSTRACT.....	x
Chapter	
1. INTRODUCTION	1
Significance of Corneal Fibrosis	
The Myofibroblast: Corneal Wound’s Friend and Corneal Transparency’s Foe	
Molecular Mechanisms of Corneal Wound Healing: The Role of TGF-β1	
Use of Histone Deacetylase Inhibitors to Prevent Corneal Fibrosis	
Need for Novel Model of Canine Corneal Fibrosis	
2. EXPERIMENTAL PURPOSE AND HYPOTHESES	7
3. MOLECULAR MECHANISMS OF SUBEROYLANILIDE HYDROXAMIC ACID (SAHA) IN THE INHIBITION OF TGF-B1 MEDIATED CANINE CORNEAL FIBROSIS	9
Materials and methods	
Results	
Discussion	
Conclusion	
4. EFFICACY OF SUBEROYLANILIDE HYDROXAMIC ACID (SAHA) IN NOVEL <i>IN VIVO</i> MODEL OF CANINE CORNEAL FIBROSIS	19
Materials and methods	
Results	

Discussion

Conclusion

APPENDIX

1. TABLES48

2. FIGURES51

3. COPYRIGHT RELEASE.....59

BIBLIOGRAPHY.....61

VITA.....70

LIST OF TABLES

Tables

1. Sequence of primers for detecting MMP RNA	48
2. Tissue targets of special histopathology stains	48
3. Scoring system for severity of corneal neovascularization, edema and staining.....	48
4. Possible orientation patterns based on the value of eigenvalues λ_1, λ_2 of the Hessian matrix ($ \lambda_1 \geq \lambda_2 $) for TEM	49
5. Epithelial and total corneal thickness measurements at baseline and following the alkali burn using OCT	49
6. Scores for severity of corneal neovascularization, edema and staining.....	49
7. Area of type I collagen, type III collagen and total collagen in the wound bed (alkali-burned corneas) and axial cornea (control cornea)	50
8. Corneal collagen fibril dimensions measured with TEM	50

LIST OF FIGURES

Figures	Page
1. Representative western blot showing the effect of SAHA +/- TGF- β 1 on Smad phosphorylation in canine corneal fibroblast (CCF) cell extracts	51
2. Representative western blot showing the effect of SAHA +/- TGF- β 1 on p38 mitogen-activated protein (MAP) kinase phosphorylation in canine corneal fibroblast (CCF) cell extracts	51
3. Representative western blot showing the effect of SAHA +/- TGF- β 1 on ERK1 and ERK2 phosphorylation in canine corneal fibroblast (CCF) cell extracts	51
4. Representative western blot showing the effect of SAHA +/- TGF- β 1 on JNK phosphorylation in canine corneal fibroblast (CCF) cell extracts	52
5. Graph showing real time qPCR mRNA quantification of matrix metalloproteinases (MMPs) 1, -2 and -9 in canine corneal fibroblasts (CCF).....	52
6. Representative gelatin zymography demonstrating the effect of SAHA +/- TGF- β 1 on MMP2 and MMP9 protein expression in canine corneal fibroblast (CCF) cell extracts	53
7. Various TEM modules used to analyze collagen fibril size and organization. Representative normal canine cornea. A) Original TEM image. B) Collagen fibril segmentation results. D) Fibril centroids and fibril neighborhood graph. D) Nearest (red) and farthest (blue) immediate neighbors.....	53
8. Clinical scores and corneal haze grades following the 20 second alkali burn in a representative dog. A) One day following alkali burn, the mMS score was 17.5 and corneal haze grade was 3. B) On day 5 the mMS score was 11 and corneal haze grade was 2. C) Ten days post-alkali burn the mMS score was 8.5 and corneal haze grade was 2. D) At the study's endpoint (day 14), the mMS score was 6.5 and corneal haze grade was 2.....	54
9. Representative OCT images of normal cornea at baseline and alkali-burned cornea 14 days after wounding. A) Normal cornea of a dog prior to wounding. The values in green represent epithelial and total corneal thickness. B) Alkali-burned cornea from dog in treatment group A. C) Alkali-burned cornea from dog in treatment group B. Note the variable epithelial thickness and the increased total corneal thickness in the alkali-burned cornea compared to the normal cornea at baseline.	55
10. Representative histological images of normal (A-D) and alkali-burned corneas (E-H). H&E stain demonstrated an increased cellularity of the anterior stroma in the alkali-burned corneas (E) compared to normal corneas (A). Masson's	

trichrome stain of the alkali-burned cornea (F) confirmed presence of mesenchymal cells in the anterior stroma, which are absent in normal cornea (B). The formation of elastic fibers was demonstrated in the alkali-burned cornea with EVG (G). No elastic fibers were detected in normal cornea (C). PAS stained corneas showed increased basement membrane and fibrin deposition in the alkali-burned cornea (H) compared to normal cornea (D)56

11. Representative Picrosirius red stained negative control (A) and alkali-burned (B) corneas. Note the increased amount of type III collagen fibers in the alkali-burned cornea compared to the negative control. This transition of type I to type III collagen fibers is typical of scar formation.....56
12. Representative immunohistochemistry of normal (A) and alkali-burned (B) corneas. Increased α -smooth muscle actin stain in the alkali-burned corneas confirmed the cell population in the anterior stroma as fibroblasts. There was only a mild-moderate increase in CD18 stain in the alkali-burned cornea indicating that the majority of the cellular infiltrate was not inflammatory in nature.....57
13. Representative transmission electron microscopy images of normal cornea (A) and alkali-burned (B) corneas, specifically measuring the minimum and maximum interfibrillar distances. Note the increased minimum (red) and maximum (blue) interfibrillar distances in the alkali-burned cornea compared to normal cornea.....58

LIST OF ABBREVIATIONS

1. SAHA: Suberanolhydroxamic Acid
2. TGF- β : Transforming growth factor- β
3. ECM: Extracellular matrix
4. MMP: Matrix metalloproteinase
5. α -SMA: α -Smooth muscle actin
6. MAPK: MAP kinase
7. PRK: Photorefractive keratectomy
8. R-Smads: Receptor-regulated Smads
9. Co-Smads: common mediator Smads
10. I-Smads: inhibitor Smads
11. HDAC: *Histone deacetylase*
12. HAC: Histone acetyltransferase
13. HDACi: Histone deacetylase inhibitors
14. CCF: Canine corneal fibroblasts
15. PCR: Polymerase chain reaction
16. DMSO: Dimethyl sulfoxide
17. OCT: Optical coherence tomography
18. IHC: Immunohistochemistry
19. TEM: Transmission electron microscopy
20. H&E: Hematoxylin and eosin
21. EVG: Elastica-van Gieson
22. PAS: Periodic acid-Schiff

ABSTRACT

Purpose: The aims were to (1) investigate the molecular mechanisms mediating the anti-fibrotic effect of SAHA in the canine cornea using an *in vitro* model and (2) to develop a novel *in vivo* model of corneal fibrosis in dogs utilizing alkali burn and assess the ability of SAHA to inhibit fibrosis using this canine model.

Methods: In study 1, canine corneal fibroblasts were incubated for 24hrs +/- Transforming Growth Factor- β 1 (TGF- β 1) and SAHA. Western blot was used to quantify isoforms of intracellular signaling proteins. Real-time PCR and zymography quantified matrix metalloproteinases (MMP) mRNA and protein expression, respectively. In study 2, a corneal alkali burn was created in Beagles using 1 N NaOH topically. Dogs were randomly and equally assigned into 2 groups: A) vehicle (DMSO); B) anti-fibrotic treatment (SAHA). Degree of corneal opacity and efficacy of SAHA were determined utilizing the Fantes grading scale, optical coherence tomography, corneal histopathology, immunohistochemistry and transmission electron microscopy.

Results: In study 1, SAHA treatment reduced phosphorylation of Smad2/3, ERK1/2 and altered MMP protein and gene expression. In study 2, α -smooth muscle staining and minimum and maximum interfibrillar distances were significantly greater in burned corneas.

Conclusion: Corneal anti-fibrotic effects of SAHA involve modulation of canonical and non-canonical components of TGF- β 1 intracellular signaling and MMP activity. The alkali burn generates corneal opacity without damaging the limbus, and induces reliable fibrosis. Additional *in vivo* SAHA dosing studies with larger sample size are warranted.

CHAPTER 1

INTRODUCTION

Significance of Corneal Fibrosis

Ocular injury threatens short and long-term corneal clarity and vision. Both human and veterinary patients are commonly subject to corneal injury, the cause of which may be pathologic (e.g. trauma, infection, other) or surgical (e.g. status post corneal transplant or photorefractive keratectomy (PRK), conjunctival grafting procedures, other).¹⁻⁴ Regardless of the exact etiology the resulting sequela is often loss of corneal transparency due to dysregulated healing and subsequent fibrosis.⁵ Corneal fibrosis can result in blindness, rendering a person unable to read, write, operate a vehicle and perform other required daily tasks. Similarly, corneal fibrosis is debilitating to veterinary patients. The loss of corneal transparency impairs the animal's visual field and depth perception resulting in decreased performance. For example, an affected German Shepherd dog is unable to execute search and rescue operations, a Golden Retriever working as a guide dog for the blind is no longer able to assist its owner, or a horse cannot compete in flat races, polo sports, or show jumping. As a consequence of this inability to perform, an animal may be immediately and prematurely retired or potentially even euthanized, especially when the blind animal is deemed a danger to people. The loss of animals suffering from corneal fibrosis is emotional (e.g. to trainers and owners) and financially devastating (e.g. service dogs are significant investments for government and not-for profit programs; equine athletes are an integral part of the equestrian sports industry which accrues approximately a billion dollars annually). Corneal fibrosis remains one of the leading causes of blindness in animals and people worldwide.^{6,7} Thus,

the development of novel, successful strategies to treat corneal fibrosis remains an important goal among both physician and veterinary ophthalmologists.

The Myfibroblast: Corneal Wound's Friend and Corneal Transparency's Foe

Corneal wound healing is a complex process that involves the signaling of numerous cytokines, up-regulation of matrix metalloproteinases (MMPs), increased deposition of extracellular matrix (ECM), activation of keratocytes, and subsequent formation of both fibroblasts and myofibroblasts (i.e. epithelial to mesenchymal transdifferentiation).⁸⁻¹³ Myofibroblasts are contractile, metabolically active, opaque cells containing intracellular microfilament bundles of F-actin, desmin, vimentin and α -smooth muscle actin (α -SMA), and so myofibroblasts are able to cause wound contracture, restore the ECM and create intercellular adhesions. Consequently myofibroblasts are the ideal cell type for corneal wound repair. However, this process also results in a loss of corneal transparency as the ECM deposited by the myofibroblasts and the myofibroblasts themselves are opaque.¹⁴ Typically, the corneal opacification resolves with disappearance of the myofibroblasts and reabsorption of the opaque ECM. Disappearance of myofibroblast likely occurs either (1) through reversion of the myofibroblast back to keratocytes, which has been demonstrated *in vitro*¹⁵ or (2) by apoptosis. It is believed that apoptosis of myofibroblasts is mediated by restoration of corneal epithelial basement membrane as with the return of the basement membrane, the epithelial-derived cytokine, Transforming Growth Factor- β (TGF- β), can no longer penetrate the anterior stroma and perpetuate the myofibroblast phenotype.^{14,16} It is this particular cytokine which drives the transformation of fibroblast to myofibroblast and thus TGF- β has earned the title: “master of fibrosis”.¹⁷

Molecular Mechanisms of Corneal Fibrosis: The Role of TGF- β 1

Many different cytokines are produced in response to corneal wounding and of these various cytokines TGF- β has been shown to play a major role in the formation of corneal fibrosis.^{9,18,19}

Three isoforms of TGF- β have been detected in the mammalian cornea, specifically TGF- β 1, TGF- β 2 and TGF- β 3.²⁰ These members of the TGF- β family are homologous proteins. Structurally, the active forms of each isoforms are homodimer proteins with a molecular weight of 25 kDa. Genetically, TGF- β 1 and TGF- β 2 share approximately 70% of their amino acid sequences while TGF- β 1 and TGF- β 3 share 76% of their amino acid sequences, and amino acid sequences of TGF- β 2 and TGF- β 3 are 80% compliant.²¹ However, despite their structural and genetic similarities, each isoform is encoded by genes which are located in different regions of different chromosomes.²²⁻²⁴ Thus, each isoform is allowed to possess individual and distinct functions.^{21,25} For instance, it has been made evident that both TGF- β 1 and TGF- β 2 play critical roles in the development of corneal fibrosis^{5,26-30} while TGF- β 3 appears to inhibit fibrosis as corneal wounds treated with TGF- β 3 not only lack markers of fibrosis such as α -SMA and have a low type III: type I collagen ratio but also generate an ECM that mimics normal cornea.³¹

The effects of TGF- β are known to be mediated by various intracellular signaling pathways such as the Smad-dependent intracellular signaling pathways.^{32,33} The Smad protein family is classified based on function and is composed of three categories including receptor-regulated Smads (R-Smads), common mediator Smads (co-Smads), and inhibitor Smads (I-Smads). R-Smads possess ligand specificity and become phosphorylated after directly binding to the TGF- β Receptor. Co-Smads are needed for

nuclear entry and consequently allow for signal transduction from the cell membrane to the nucleus. Finally, I-Smads interfere with the activation of R-Smads by inhibiting their phosphorylation. Interactions among these Smad proteins ultimately results in the transformation of quiescent corneal keratocytes into corneal fibroblasts and subsequently myofibroblasts.^{18,33,34}

Although Smad proteins seem to play a primary role in TGF- β signal transduction, literature suggest that several other signaling pathways also allow for TGF- β to modulate gene expression and cell function. For example, TGF- β 1 can activate several mitogen-activated protein kinases (MAPKs) such as ERK, JNK and p38 MAPK.³³ These MAPK pathways appear to play to a role in epithelial and endothelial cell migration in the corneas of mice, rabbits and humans. They also alter the expression of ECM genes.³⁵⁻³⁷

TGF- β is known to induce fibrosis not only through cellular transdifferentiation but also through the modulation of the activity of MMPs.³³ MMPs are proteolytic enzymes, which play a major role in extracellular matrix degradation. Physiologically, MMPs allow for remodeling of the extracellular matrix which is a necessary component of the wound repair process. However, excessive and uninhibited activity of MMPs in the cornea such as MMP2 and MMP9 can result in keratomalacia and potentially fibrinogenesis.³⁸ Overactivity of MMP1 has been implicated in ophthalmic disease as well, such as superior limbic keratoconjunctivitis and viral keratitis in people.^{39,40} Various studies have demonstrated TGF- β 1 can cause the up-regulation of the gene and protein expression of MMP1, MMP2 and MMP9.^{12,13,41-44}

It has been demonstrated that Smad and MAPK mediated gene expression is influenced by histone acetylation.⁴⁵⁻⁴⁸ Histone acetylation is controlled by the

interactions of two enzymes, histone deacetylase (HDAC) and histone acetyltransferase (HAT).⁴⁹ The activities of these two enzymes regulate gene expression and cellular function by modifying core histones or non-histone proteins.⁴⁹ HDACs have been shown to participate in the development of fibrosis within various organs, including the cornea.^{50,51} Thus, inhibition of HDAC activity represents a means by which TGF- β mediated corneal fibrosis can be reduced or prevented.⁵²⁻⁵⁵

Use of Histone Deacetylase Inhibitors to Prevent Corneal Fibrosis

The therapeutic potential of histone deacetylase inhibitors (HDACi) as anti-fibrotic agents has demonstrated extreme promise in different models of corneal fibrosis. For instance, trichostatin A, an inhibitor of class I and II HDACs, was shown to effectively decrease corneal fibrosis in rabbits, following PRK.⁵⁶ However, trichostatin A is not commercially available. A derivative of trichostatin A, suberanilohydroxamic acid (SAHA), is approved by the FDA, and recent studies by our laboratory have demonstrated its ability to not only prevent TGF- β 1-mediated fibrosis in canine and equine cornea *in vitro* but also reduce corneal haze in rabbits *in vivo*.⁵⁷⁻⁵⁹ The precise mechanism by which SAHA decreases corneal fibrosis remains undefined and clinical use of SAHA as an anti-fibrotic agent demands translational research utilizing an *in vivo* model comparable to the human cornea.

Need for Novel Model of Canine Corneal Fibrosis

Small laboratory animal species such as rodents and rabbits are commonly used in current corneal fibrosis research.^{60,61} While these *in vivo* studies overcome the limitations of *in vitro* experiments by representing native corneal wound healing, the cornea of rats, rabbits and mice differ significantly from those of people in terms of

thickness and diameter.⁶² An animal model possessing corneal anatomy and physiology similar to people is important for determining bench-to-bedside translational potential of anti-fibrotic treatments to clinical application in human and veterinary clinics. The dog represents a more optimal model than rodents or rabbits for studying molecular mechanisms mediating corneal fibrosis and testing the efficacy and safety of therapies for corneal scarring and restoring vision. Not only are the dog's corneal dimensions comparable to people,⁶² they are common veterinary patients presenting with ocular injuries that result in corneal fibrosis.⁶³ Therefore, developing a model of corneal fibrosis and discovering a successful anti-fibrotic agent in dogs would impact both physician and veterinary ophthalmology.

At this time, there is only one established *in vivo* model of canine corneal fibrosis of which the author is aware.⁶⁴ This model created by Bentley *et. al.* requires repeated epithelial debridements and therefore takes significant time to produce fibrosis. Additionally corneal haze generated with this model is not grossly appreciable. Other current *in vivo* models of corneal fibrosis used to investigate anti-fibrotic agents in small laboratory species utilize various methodologies such as sulfur mustard exposure, laceration and suture, and alkali burn.⁶⁵⁻⁶⁷ The alkali burn is easy to perform, does not require specialized equipment and presents minimal risk to those performing the procedure. It also results in significant fibrosis and neovascularization. To our knowledge, the current literature lacks a study describing the use of the alkali burn to create corneal fibrosis in dogs.

CHAPTER 2

EXPERIMENTAL PURPOSE AND HYPOTHESIS

HDACi such as SAHA have been shown to be an effective anti-fibrotic agent in equine and canine cornea *in vitro* and rabbit cornea *in vivo*, respectively.⁵⁷⁻⁵⁹ Despite these positive results, the molecular mechanisms by which SAHA prevents corneal fibrosis remain undetermined. Additionally, as the transition is made from bench top research to bedside medicine, the efficacy of SAHA needs to be evaluated in a large animal with corneal anatomy and structure that resembles that of humans, such as the dog.⁶² In study 1, we investigated the molecular mechanisms mediating the anti-fibrotic effect of SAHA in the canine cornea using an *in vitro* model. Cultured canine corneal fibroblasts (CCF) were incubated in the presence/absence of TGF- β 1 (5ng/ml) and SAHA (2.5 μ M) for 24hrs. Western blot analysis was used to quantify non-phosphorylated and phosphorylated isoforms of Smad2/3, p38 MAPK, ERK1/2 and JNK1. Real-time PCR and zymography were utilized to quantify MMP1, MMP2, MMP8 and MMP9 mRNA expression and MMP2 and MMP9 protein activity, respectively. We hypothesized that SAHA attenuates corneal fibrosis by modulating Smad-dependent and, to a lesser extent, Smad-independent signaling pathways activated by TGF- β 1, as well as MMP activity.

In study 2, we sought to develop a novel *in vivo* corneal model of fibrosis in dogs utilizing alkali burn and assess the ability of SAHA to inhibit corneal fibrosis using this large animal model. Seven research Beagle dogs were used to establish corneal opacity. An axial corneal alkali burn was created using 1 N NaOH topically. Six dogs were randomly and equally assigned into 2 groups: A) vehicle (Dimethyl sulfoxide (DMSO)), 2

$\mu\text{L}/\text{mL}$); B) anti-fibrotic treatment ($50 \mu\text{M}$ SAHA). Degree of corneal opacity, ocular health, and efficacy of SAHA were determined utilizing the Fantes grading scale, modified McDonald-Shadduck (mMS) scoring system, optical coherence tomography (OCT), corneal histopathology, immunohistochemistry (IHC), and transmission electron microscopy (TEM). We hypothesized that the corneal alkali burn would create significant focal corneal fibrosis and that SAHA would reduce the severity of the corneal fibrosis in the canine cornea.

CHAPTER 3

STUDY 1: MOLECULAR MECHANISMS OF SUBEROYLANILIDE HYDROXAMIC ACID (SAHA) IN THE INHIBITION OF TGF-B1 MEDIATED CANINE CORNEAL FIBROSIS¹

¹ Gronkiewicz, K. M., Giuliano, E. A., Sharma, A. and Mohan, R. R. (2015), Molecular mechanisms of suberoylanilide hydroxamic acid in the inhibition of TGF- β 1-mediated canine corneal fibrosis. *Veterinary Ophthalmology*. doi: 10.1111/vop.12331

Materials and methods

Canine corneal fibroblast (CCF) cultures

Primary canine corneal fibroblast cultures were established following the protocol previously described.^{58,68} Briefly, full-thickness 6 mm axial corneal buttons were aseptically harvested from 3 dogs euthanized for reasons unrelated to the study. These purpose-bred, university owned, research dogs were being sacrificed for an orthopedic study in which they were enrolled. Eyes were examined by slit-lamp biomicroscopy prior to euthanasia and determined to be free of anterior segment disease. The corneal biopsies were washed with sterile minimal essential medium (MEM, Gibco, Grand Island, NY, USA), and the epithelium and endothelium were removed with careful dissection using a number 10 blade (BD, Franklin Lakes, NJ, USA). The remaining corneal stroma was sub-sectioned and placed in 100x20 mm tissue culture dishes (BD, BioSciences, Durham, NC, USA) containing MEM supplemented with 10% fetal bovine serum. These stromal explants were then incubated in a humidified 5% CO₂ incubator at 37°C to obtain CCF cultures. The primary CCF harvested from the corneal stromal sub-sections were seeded into 100x20 mm tissue culture plates in MEM supplemented with 10% fetal bovine serum and allowed to reach 80% confluence.

TGF- β 1 and SAHA treatment

A 10 mM stock solution of SAHA (Cayman Chemical Company, Ann Arbor, MI) was made using dimethylsulfoxide (DMSO) and diluted 4000 times with MEM to achieve a final concentration of 2.5 μ M. Upon reaching 80% confluence CCF were exposed to either TGF- β 1 (5 ng/ml) or SAHA (2.5 μ M) alone or both for 24 hours.

Immunoblotting

Protein lysates were harvested from CCF using a radioimmunoprecipitation assay (RIPA) lysis buffer containing a protease inhibitor cocktail (Santa Cruz Biotechnology, Santa Cruz, CA). The samples were then centrifuged at 10,000 g for 10 min. Following centrifugation, samples were suspended in NuPAGE LDS buffer containing a reducing agent (Life Technologies Corporation, Grand Island, NY, USA) and heated at 70°C for 10 min. Proteins were resolved by NuPAGE Novex Bis-Tris mini gels (Life Technologies, Invitrogen, Grand Island, NY, USA) and were transferred onto the polyvinylidene difluoride membranes utilizing overnight wet transfer technique at 25 volts. To detect transferred proteins, the membranes were then incubated with the following primary antibodies: p38 MAPK, phospho-p38 MAPK, JNK1, phospho-JNK1, ERK1/2, phospho-ERK1/2 (Cell Signaling, Beverly, MA, USA), Smad2/3 and phospho-Smad2/3 (Santa Cruz biotechnology Inc., Dallas, TX, USA). Membranes were then washed and incubated with alkaline phosphatase conjugated anti-mouse, anti-goat, or anti-rabbit secondary antibody. After washing three times in Tris-buffered saline for 5 minutes, membranes were developed using the nitroblue tetrazolium/5-bromo-4-chloro-3-indolylphosphate method. All western blots for each protein were repeated at least two times. Digital quantification of western blots was performed using Image J software (NIH, Bethesda, MD, USA).

RNA extraction, cDNA synthesis and PCR

Total RNA was extracted from CCF with RNeasy kit (Qiagen, Valencia, CA). The RNA was then reverse transcribed to cDNA following vendor's instructions (Promega, Madison, WI). Real-time PCR was performed to detect and quantify MMP1, MMP2, MMP8 and MMP9 mRNA using the Step One Plus real-time PCR system (Life

Technologies, Grand Island, NY, USA). A 20 μ l reaction mixture containing 2 μ l of cDNA, 2 μ l of forward primer (200 nM), 2 μ l of reverse primer (200 nM), and 10 μ l of 2X SYBR green super mix (Bio-Rad Laboratories, Hercules, CA) was run at a universal cycle (95 °C for 10 min, 40 cycles at 95 °C for 15 s, and 60 °C for 60 s) in accordance with the manufacturer's instructions as reported earlier.⁵⁸ β -Actin was used as the housekeeping gene. Each PCR reaction was run in triplicate and repeated at least 2 times. The primer sequences used in PCR analysis are listed in Table 1.

Zymography

Gelatin zymography was used to quantify pro and active isoforms of MMP2 and MMP9 proteins. The 10% Novex pre-cast SDS polyacrylamide gels (Life Technologies, Novex, Carlsbad, CA, USA) in the presence of 0.1% gelatin were used under non-reducing conditions. A 20 μ L zymography sample was prepared by mixing total protein lysates (30 μ g), Tris-Glycine SDS sample buffer (10 μ L) and deionized water (0-6 μ L). Protein standards were run concurrently to identify molecular weight. Samples were loaded for SDS-PAGE with 1X Tris-Glycine SDS Running Buffer and were run at a constant voltage (125 Volt) for 120 minutes without heating. Following completion of electrophoresis, the gel was washed once in 1X Zymogram Renaturing Buffer, which was then decanted, and the gel was next washed twice with 1X Zymogram Developing Buffer. For the second washing, the gel was incubated at 37 °C overnight. For staining, the gel was washed with Simply Blue Safe stain diluted with deionized water (1:2) for 60 minutes. The stain was then decanted and the gel was washed in deionized water for 24 hours. Three separate zymograms were performed for each treatment group. Digital quantification of zymograms was performed using NIH Image J software.

Statistical analyses

Results were expressed as a mean \pm standard error. One-way analysis of variance (ANOVA) and Tukey's test post-hoc were used to statistically analyze results, and $p < 0.05$ was considered significant.

Results

Effects of SAHA on TGF- β 1-induced Smad phosphorylation

As presented in Fig. 1, TGF- β 1 treatment of CCF caused a 2.8 ± 0.28 fold ($p < 0.01$) increase in Smad2/3 phosphorylation. Conversely, expression of phospho-Smad2/3 in CCF exposed to both SAHA and TGF- β 1 was unchanged and comparable to untreated controls. These results suggested that SAHA significantly ($p < 0.01$) attenuated TGF- β 1-induced Smad2/3 phosphorylation.

Effects of SAHA on TGF- β 1-induced MAPK

In Fig. 2, the effect SAHA and/or TGF- β 1 on the phosphorylation of p38 MAPK are displayed. TGF- β 1 caused a 3.5 ± 0.66 fold ($p < 0.05$) increase in p38 MAPK phosphorylation. SAHA treatment partially attenuated TGF- β 1-induced p38 MAPK phosphorylation down to 2.4 ± 0.4 fold; however, SAHA treatment did not significantly attenuate TGF- β 1-induced p38 MAPK phosphorylation, suggesting that modulation of p38 MAPK signaling may not be primarily involved in the mechanism of action of SAHA.

Next, the effect of TGF- β 1 and SAHA on ERK1/2 and JNK1 signaling were investigated. As demonstrated by Fig. 3, TGF- β 1 treatment alone did not alter the phosphorylation of ERK1/2. On the other hand, CCF exposed to SAHA alone or in combination with TGF- β 1 showed significantly reduced expression of phospho-ERK1

(2.7 ± 0.6 fold decrease $p < 0.01$) and phospho-ERK2 (8.0 ± 3.0 fold decrease $p < 0.05$). These results suggested that SAHA treatment inhibited ERK1/2 phosphorylation, regardless of concurrent-treatment with TGF- β 1.

Thereafter, we tested the effects of SAHA on JNK1 signaling. Phospho-JNK1 expression was not detected in the untreated control CCF. Similarly, neither TGF- β 1 nor SAHA alone or in combination with TGF- β 1 showed any change on phospho-JNK1 expression. These results are displayed in Fig. 4.

Effects of SAHA on MMP mRNA and protein expression

Real time PCR was used to quantify the effect of SAHA and/or TGF- β 1 on MMP gene expression in CCF. As shown in Fig. 5, TGF- β 1 caused a 6.0 fold ($p < 0.01$) increase in MMP1 mRNA and 10.0 fold ($p < 0.01$) increase in MMP9 mRNA expression, but did not have a significant effect on MMP2 mRNA expression. SAHA treatment alone did not alter MMP1, MMP2 or MMP9 expression. However, concurrent SAHA and TGF- β 1 treatment caused a significant increase in MMP1 mRNA ($p < 0.05$) and a significant decrease in the MMP9 mRNA ($p < 0.05$) expression. Real time PCR performed to quantify MMP8 mRNA did not detect any change in MMP8 mRNA in untreated control CCF or SAHA or TGF- β 1 treated CCF.

Gelatin zymography was performed to detect the protein isoforms of MMP2 and MMP9; and results are presented in Fig. 6. MMP2 and MMP9 proteins were detected in untreated control CCF and this expression remained unaltered after TGF- β 1 treatment. Treatment of SAHA alone or in combination with TGF- β 1 caused a significant increase in both MMP2 (1.5 ± 0.01 fold increase $p < 0.05$) and MMP9 (3.0 ± 0.77 fold increase $p < 0.05$) protein expression.

Discussion

Our group has demonstrated the anti-fibrotic potential of HDACi, specifically trichostatin A (TSA) and SAHA, in various models of corneal fibrosis.^{56,58,59} Sharma *et al.* found that TSA not only inhibited TGF- β 1-induced α -SMA, fibronectin and myofibroblast formation in human corneal fibroblasts *in vitro* but also significantly decreased corneal haze in rabbits *in vivo* following photorefractive keratectomy.⁵⁶ Recently, Bosiack *et al.* determined that SAHA inhibited canine corneal fibrosis *in vitro*,⁵⁸ and Tandon *et al.* demonstrated the anti-fibrotic properties of SAHA *in vivo*, also utilizing rabbits which had undergone photorefractive keratectomy.⁵⁹ However, these studies did not detail the mechanism(s) of action of HDACi as corneal anti-fibrotic agents. To the best of our knowledge, the molecular mechanisms of the anti-fibrotic effects of SAHA in the cornea is largely unknown.⁶⁹

The results of this study suggest that SAHA prevents canine corneal fibrosis through many different mechanisms including the modulation of TGF- β 1-induced pro-fibrotic intracellular signaling pathways. Smad proteins largely mediate the intracellular signaling triggered by TGF- β 1. R-Smads, such as Smad2 and Smad3, are considered pro-fibrotic intracellular signaling molecules. Consequently, these Smad proteins represent intracellular therapeutic targets for the manipulation of TGF- β 1 mediated fibrosis. The inhibition of TGF- β 1-induced phosphorylation of Smad2 and Smad3 has been demonstrated in models of renal, hepatic, cardiac and pulmonary fibrosis.⁷⁰⁻⁷³ Previous studies from our laboratory utilizing RNAi-mediated knock down models have shown that TGF- β 1-mediated Smad2/3 phosphorylation is an essential step for fibroblast transdifferentiation to myofibroblasts.⁷⁴ Therefore, it was hypothesized that SAHA may

inhibit corneal fibrosis by attenuating TGF- β 1-induced phosphorylation of Smad2/3. In the present study, SAHA significantly attenuated TGF- β 1-induced phosphorylation of Smad2/3, thereby confirming our initial hypothesis that the inhibition of TGF- β 1-induced phosphorylation of these R-Smads plays an important role in the anti-fibrotic effects of SAHA in the canine cornea.

Although Smad intracellular signaling serves as the canonical pro-fibrotic pathway of TGF- β 1, it has been demonstrated that TGF- β 1 also induces fibrosis through other intracellular signaling molecules. Previous *in vitro* and *in vivo* models of cardiac, renal and corneal fibrosis demonstrated TGF- β 1 induces the phosphorylation of p38 MAPK,⁷⁵⁻⁷⁷ thereby supporting the results of this study, wherein treatment of CCF with TGF- β 1 caused a marked increase in the phosphorylation of p38 MAPK. In contrast, treatment of CCF with TGF- β 1 for 24 hours did not significantly modulate the phosphorylation of ERK1/2 or JNK1. These results are in accordance with previous studies which demonstrated that TGF- β 1 caused only a transient increase in ERK and JNK phosphorylation, the expression of which returned to baseline after 1 hour of treatment.^{77,78}

In this study, the effects of SAHA on TGF- β 1-induced phosphorylation of the various MAPKs appeared to be subtype-specific. For example, SAHA caused a significant reduction in the phosphorylation of ERK1/2. As previously stated, TGF- β 1 causes a transient increase in ERK1/2 phosphorylation, and so the observed attenuation of ERK1/2 phosphorylation by SAHA appears to be a means by which SAHA inhibits corneal fibrosis. However, SAHA did not affect the phosphorylation of p38 MAPK or JNK1, suggesting that these two MAPKs are not involved in the anti-fibrotic mechanisms

of SAHA in the cornea. These results conflict with those of previous studies which demonstrated the ability of HDACi, including SAHA, to inhibit phosphorylation of p38 MAPK in neoplastic cells, rheumatoid arthritis synovial fibroblast and lens epithelial cells.⁷⁹⁻⁸¹ It is important to note that these studies utilized cytokines different than TGF- β 1 to induce cellular transformation and fibrosis. Therefore, it may be possible that TGF- β 1 induces the phosphorylation of p38 MAPK through means which are inaccessible to SAHA, or SAHA may be able to prevent the phosphorylation of p38 MAPK in canine corneal fibroblasts in the presence of a different corneal cytokine, such as interleukin 1 β (IL-1 β), Platelet Derived Growth Factor (PDGF) or Connective Tissue Growth Factor (CTGF). Future studies would investigate these potential effects of SAHA in an *in vitro* model of canine corneal fibrosis utilizing different inflammatory cytokines.

It has been well established that MMPs play a critical role in the degradation and subsequent remodeling of the extracellular matrix. Past studies have consistently shown that TGF- β 1 causes increased expression of MMP1 and MMP9 mRNA in corneal cells *in vitro*.^{12,13,82} Our study's data support previous findings, as TGF- β 1 treatment resulted in the increased expression of MMP1 and MMP9 mRNA. While TGF- β 1 treatment for 24 hours did not affect MMP2 mRNA in the present study, Donnelly *et. al.* demonstrated that TGF- β 1 treatment for 5 days caused a significant increase in MMP2 mRNA.⁵⁷ When analyzing the effects of TGF- β 1 on MMP protein expression, no significant changes were noted in the expression of MMP2 or MMP9 proteins. These results suggest that prolonged exposure to TGF- β 1 may be necessary to alter MMP protein expression in CCF. Alternatively, it may be possible that TGF- β 1 may not be involved in the

expression of MMP protein, as previously demonstrated by a study in which both normal and keratoconic human corneal keratocytes were treated with TGF- β 1 for 7 days.⁸³

Several studies have investigated the effects of different HDACi on MMPs in various cell types and the results appear to be drug-, dose- and tissue-specific.⁸⁴⁻⁸⁷ Treatment with SAHA alone did not significantly affect MMP1, MMP2 or MMP9 mRNA in our investigation of CCF. However, treatment with both SAHA and TGF- β 1 significantly increased MMP1 mRNA, decreased MMP9 mRNA and had no effect on MMP2 mRNA. Unexpectedly, CCF treated with either SAHA alone or SAHA and TGF- β 1 expressed significantly increased expression of MMP9 protein, despite the aforementioned decreased MMP9 mRNA expression within the same treatment group. We speculate that SAHA may affect cellular proteins involved in MMP9 degradation, thus increasing the half-life of this particular MMP. Overall, our data suggest that modulations of MMP expression by HDACi is not only isoform specific but also may be affected by other inducible inflammatory cytokines and growth factors.

Conclusion

In summary, this study is the first report to the authors' knowledge investigating both the pro-fibrotic intracellular signaling cascade in canine corneal fibroblast induced by TGF- β 1 and the molecular mechanisms of action of SAHA as a corneal anti-fibrotic agent. Results indicate that SAHA affects both canonical and non-canonical components of the TGF- β 1 intracellular signaling pathways and pathways independent of TGF- β 1. Finally, SAHA alters both gene and protein expression of MMP2 and MMP9. However, the mechanisms of these modulations and their clinical significance need further investigation.

CHAPTER 4

STUDY 2: EFFICACY OF SUBEROYLANILIDE HYDROXAMIC ACID (SAHA) IN NOVEL *IN VIVO* MODEL OF CANINE CORNEAL FIBROSIS²

APPENDIX 3: COPYRIGHT RELEASE OF PUBLISHED MANUSCRIPT FOR USE IN THESIS

²Gronkiewicz, K.M., Giuliano, E.A., Kuroki, K., Bunyak, F., Sharma, A., Teixeira, L.B.C., Hamm, C.W., Mohan R.R. Development of a novel in vivo corneal fibrosis model in the dog, *Experimental Eye Research*, Volume 143, February 2016, 75-88

Material and methods

Animals

Seven healthy female Beagle dogs (9-12 months, 10-15 kg) were purchased from Covance Laboratory (Cumberland, VA) and housed in a research facility at the University of Missouri. Prior to the onset of the study all dogs underwent a complete ophthalmic examination by a board certified veterinary ophthalmologist (EAG) which included slit lamp biomicroscopy (SL-15 Kowa Company, Ltd, Tokyo, Japan), indirect ophthalmoscopy (Wireless indirect ophthalmoscope, Keeler Instruments Inc., Broomall, PA, USA and pan retinal 2.2 indirect lens, Volk Optical Inc., Mentor, OH, USA), Schirmer tear test I (Schering-Plough Animal Health, Union, NJ, USA), tonometry (Tono-Pen Vet, Dan Scott and Associates, Westerville, OH, USA) and fluorescein staining (Flu-Glo, Akorn, Inc., Buffalo Grove, IL, USA). All dogs were determined to be free of ocular disease. The dogs received daily socialization and all other husbandry needs including a diurnal 12 hour light cycle. All studies were performed in accordance with the ARVO Statement for the Use of Animals in Ophthalmic and Vision Research and were approved by the University of Missouri Institutional Animal Care and Use Committee.

Baseline Anterior Segment OCT

Imaging was performed with a Heidelberg Spectralis® OCT (Heidelberg Engineering, Heidelberg, Germany) which was equipped with an Anterior Segment Module attachment to shift the focal plane from the retina to the cornea. The Heidelberg system functions at 815 nm and can perform 40,000 A-scans per second. The

imaging unit has a working distance of 11-14 mm, depending on the axial length of the eye and the type of pathology being imaged.

To obtain baseline OCT images, animals were sedated with dexmedetomidine (Zoetis Inc., Kalamazoo, MI, USA, 7 mcg/kg, IM). They were then placed and maintained in sternal recumbancy with gentle manual restraint. A 6 mm corneal pachymetry protocol was performed by a single operator (CWH). After bringing the objective lens close to the cornea, the image was aligned to the axial cornea, and only scans that were free of motion artifact were accepted for data analysis. Upon completion of OCT imaging, atipamazole hydrochloride (Zoetis Inc., Kalamazoo, MI, USA, volume equivalent to that of dexmedetomidine, IM) was administered to reverse the effects of dexmedetomidine.

Image analysis of normal corneas included measurements of both epithelial and total corneal thickness. For each image, single measurements of these parameters were made using the measurement calipers provided by the AS-OCT software.

Development of Corneal Alkali Burn in a Sentinel Dog

To effectively develop the novel model of canine corneal fibrosis *in vivo*, a sentinel dog underwent focal corneal alkali burn of each eye at separate time points. The corneal wounding was performed by a board certified veterinary ophthalmologist (EAG). The animal was sedated with dexmedetomidine (7mcg/kg, IM) and hydromorphone (0.1 mg/kg, IM). Following sterile placement of an intravenous catheter, propofol (Abbott Animal Health, Abbott Park, IL, USA, 2-4 mg/kg, IV) was administered until the animal was at an appropriate level of anesthesia for intubation. However, intubation was only considered necessary if apnea occurred, and anesthesia was maintained with IV

administration of propofol to effect. The right eye was then aseptically prepared, using a 1:20 dilution of betadine solution, and then local anesthetic medication (proparacaine hydrochloride 1%, Bausch & Lomb Inc., Tampa, FL, USA) was applied to this eye 3 times to numb the corneal surface. Topical mydriatic and cycloplegic agent (atropine sulfate 1%, Bausch & Lomb Inc., Tampa, FL, USA) was then applied once.

To perform the alkali burn, a 6 mm diameter filter paper disc was soaked in 1 N NaOH. The disc was then promptly applied to the axial cornea of the right eye for 15 seconds. Following removal of the filter paper disc the cornea was rinsed with sterile phosphate buffered saline for 60 seconds. After the cornea was thoroughly rinsed, fluorescein stain was applied topically to verify the corneal burn and resulting ulceration. Atipamazole hydrochloride (volume equivalent to that of dexmedetomidine, IM) was administered to reverse the effects of dexmedetomidine and the dog was then routinely recovered from the short anesthetic episode.

The dog received standard treatment for corneal ulceration including topical antibiotic (Bactracin, polymyxin B, gramicidin ophthalmic solution, Paddock Laboratories Inc., Minneapolis, MN, USA 1 drop OD q 8 hr), topical mydriatic and cycloplegic (atropine sulfate 1.0%, ophthalmic solution, Akorn Inc., Lake Forest, IL, USA, 1 drop to effect), systemic anti-inflammatory medication (carprofen, Zoetis Inc., Kalamazoo, MI, USA, 2.2 mg/kg PO q 12 hr) and systemic analgesic medication (tramadol, Amneal Pharmaceuticals, Bridgewater, NJ, USA, 4 mg/kg, PO q 12 hr). To prevent ocular self-trauma the dog also wore an Elizabethan collar until the study's endpoint.

Daily examinations and minimally invasive ophthalmic diagnostic testing (fluorescein stain application) were performed for 14 days. Using slit-lamp biomicroscopy, ocular health was graded according to the modified McDonald-Shadduck (mMS) scoring system. Corneal haze was assigned a numerical grade according to the Fantes grading scale (range from 0-4). Photography of the right eye was performed daily both prior to and after fluorescein stain application, using a Nikon D300S camera and AF-S DX NIKKOR 18-200mm f/3.5-5.6G ED VR II lens (Nikon Inc., Melville, NY, USA).

Once the corneal ulcer of the right eye had completely healed, the left eye underwent an alkali burn. The dog was anesthetized and the eye was surgically prepared as previously described. A 6 mm diameter filter paper disc soaked in 1 N NaOH was applied to the axial cornea of the left eye for 30 seconds and the cornea was then immediately flushed with phosphate buffered saline for 60 seconds. Fluorescein stain was topically applied confirming the presence of an ulcer. The dog then underwent identical treatment, examination, diagnostic testing and imaging as previously described for 14 days. At this end point, OCT imaging was repeated as previously described. Due to the variable thickness of the corneal epithelium following the alkali-burned, four different areas of the epithelium were measured in each image and values were averaged. A single measurement of total axial corneal thickness was obtained. Any abnormal lesions were noted and described with regards to their size and degree of reflectivity. The dog was then humanely euthanized with pentobarbital (100 mg/kg, IV) under sedation. Corneas were excised and samples were stored in appropriate media for histopathology, IHC, and TEM respectively.

Preparation of Vehicle and SAHA

Topical SAHA or vehicle were administered to the 6 additional study dogs following the corneal alkali burn. These topical agents were prepared by an individual masked to the study design. To prepare topical vehicle, 10 μL of dimethylsulfoxide (DMSO, Sigma-Aldrich Corp., St. Louis, MO, USA) was added to 2 mL of phosphate buffered saline in a sterile eye dropper bottle, labeled “A”, to achieve a final concentration of 2 $\mu\text{L}/\text{mL}$. For the preparation of topical SAHA, a 10 mM stock solution of SAHA (Cayman Chemical Company, Ann Arbor, MI, USA) was made by dissolving 1.3 grams of SAHA in 500 μL of dimethylsulfoxide (DMSO). Then, to achieve a final concentration of 50 μM , 10 μL of the 10 mM stock solution of SAHA was added to 2 mL of phosphate buffered saline in a sterile eye dropper bottle, and labeled “B”.

Corneal Alkali Burn in 6 Additional Dogs

Prior to performing the alkali burn, 6 dogs were randomly assigned to one of 2 treatment groups (3 dogs/group). Group A served as control, receiving topical vehicle in addition to the previously described standard treatment for corneal ulceration. Group B, the experimental group, received topical SAHA (50 μM) and standard treatment for corneal ulceration.

Corneal wounding was performed by a board certified veterinary ophthalmologist (EAG). To perform the alkali burn, the dogs were anesthetized, and the right eye was surgically prepared as previously described for the sentinel dog. Based on the results of the sentinel dog’s alkali burn of 15 and 30 seconds respectively, a 6 mm diameter filter paper disc soaked in 1 N NaOH was applied to the axial cornea of the right eye for 20 seconds. After the affected cornea was rinsed with phosphate buffered saline for 60

seconds fluorescein stain was topically applied. The dogs then received the standard of care for corneal ulceration and topical vehicle (Group A) or SAHA (Group B). Both vehicle and SAHA were administered q 8 hr. Elizabethan collars were worn by all dogs.

The dogs underwent daily examinations by a veterinary ophthalmologist (EAG) masked to treatment group and were scored using the mMS and Fantes grading systems. Diagnostic testing and imaging as previously described for the initial dog was performed at each examination until the study's endpoint (day 14). At study endpoint OCT imaging was repeated as previously described: four different areas of epithelium and a single total axial corneal thickness measurements were taken and any abnormal lesions were described with regards to their size and degree of reflectivity. Dogs were humanely euthanized with pentobarbital (100 mg/kg, IV) under sedation, and corneas were excised, subsectioned, and stored appropriately for histopathology, IHC and TEM. Normal corneas from 3 dogs of different breeds (Miniature Poodle, American Pit bull terrier and mixed breed dog) that were being euthanized for reasons unrelated to the study were used as negative controls for histopathology, IHC, and TEM.

Histopathological Analysis of H&E, Masson's Trichrome, Elastica van Gieson and Periodic acid-Schiff Stained Corneal Sections

Corneas were halved using sharp dissection with one section being placed in 10% buffered formalin for histopathological analysis and the other stored for TEM (see TEM methodology). After routine histologic processing, 5 µm sections were mounted on glass slides for staining with hematoxylin and eosin (H&E), Masson's trichrome, picrosirius red, elastica-van Gieson (EVG) and periodic acid-Schiff (PAS). H&E, Masson's trichrome, EVG and PAS stained slides were examined using light microscopy by a

masked, board-certified veterinary pathologist (KK). Picrosirius red slides were evaluated by a masked, board-certified veterinary pathologist (LBCT) (see next section). Corneal tissue sections were described and evaluated for any histopathological abnormalities, specifically neovascularization and edema. The severity of the neovascularization and edema on H&E and staining intensity in the anterior stroma of the Masson's trichrome, EVG and PAS stained corneas were subjectively assigned a grade from 0-3. The component of stain scored and grading scale are described in Tables 1 and 2 respectively.

Histopathological Analysis of Picrosirius Red Stained Corneal Sections

The picrosirius red stained slides were analyzed using a bright field microscope (Olympus BX43, Melville, NY). Images were captured by a mounted digital camera (Olympus DP72, Melville, NY) and analyzed using an image analysis software (CellSence Dimension 1.6, Olympus, Melville, NY). The collagen type composition of the corneal stroma was measured using picrosirius red stained sections under polarized light following previously published protocols.^{88,89} Briefly, the superficial corneal stroma of the treated areas was photographed under 400X magnification and using image analysis software the total collagen area and proportion of red-yellow-orange fibers (type I collagen) and green fibers (type III collagen) were quantified.

Immunohistochemistry

Unstained, paraffin embedded tissue sections (5 μ m) underwent immunohistochemical staining to further characterize the pathologic changes subsequent to the alkali burn by one author (KK). Antibodies used included α -SMA which is a hallmark of fibrosis (Dako, #M0851, diluted 1:300) and CD18 which is expressed by all

leukocytes (UC-Davis, #CA16.3C10, diluted 1:80). Staining intensity was assigned a grade from 0-3, with 0 representing no staining, 1 -3 representing mild, moderate, marked staining, respectively.

TEM Sample Preparation and Image Capture

All reagents for this study's TEM were purchased from Electron Microscopy Sciences and all specimen preparation was performed at the Electron Microscopy Core Facility, University of Missouri, Columbia, MO, USA. Tissues were fixed in 2% paraformaldehyde, 2% glutaraldehyde in 100 mM sodium cacodylate buffer pH=7.35. Next, fixed tissues were rinsed with 100 mM sodium cacodylate buffer, pH 7.35 containing 10 mM 2-mercaptoethanol (Sigma Aldrich, St. Louis, MO, USA) and 130 mM sucrose (further referred to as 2-ME buffer). Secondary fixation was performed using 1 % osmium tetroxide (Ted Pella, Inc. Redding, California, USA) in 2-ME buffer using a Pelco Biowave (Ted Pella, Inc. Redding, California, USA) operated at 100 Watts for 1 minute. Specimens were next incubated at 4 °C for 1 hour and then rinsed with 2-ME buffer, which was followed by distilled water. Using the Pelco Biowave, a graded dehydration series (per exchange, 100 Watts for 40 s) was performed using ethanol, transitioned into acetone, and dehydrated tissues were then infiltrated with Epon/Spurr's resin (250 Watt for 3 min) and polymerized at 60 °C overnight. Sections were cut to a thickness of 85 nm using an ultramicrotome (Ultracut UCT, Leica Microsystems, Germany) and a diamond knife (Diatome, Hatfield, PA, USA). These sections were post-stained using Sato's triple lead solution stain⁹⁰ and 5% aqueous uranyl acetate. Images were acquired with a JEOL JEM 1400 transmission electron microscope (JEOL, Peabody, MA, USA) at 80 kV on a Gatan Ultrascan 1000 CCD (Gatan, Inc, Pleasanton,

CA, USA). For each cornea, four images were acquired from different areas of the anterior stroma at a magnification of 25,000X with collagen fibrils cut in cross section for subsequent analysis.

TEM Image Analysis and Quantification

For automated quantification of corneal collagen fibrils in TEM images, an in-house image processing and analysis software was developed. This image analysis pipeline consisted of three main modules, (i) fibril detection, (ii) shape analysis and cluster decomposition, and (iii) size and interfibrillar distance analysis.

Multi-scale Hessian matrix was used to detect collagen fibrils. Hessian matrix (Equation 1) described the second order structure of local intensity variations around each point of the image $L(x,y)$, and eigenvalues $\lambda_{1,2}$ (Equation 2) of Hessian matrix was used to detect blob-like, or ridge-like structures. Table 3 shows possible local orientation patterns based on the eigenvalues of the Hessian matrix.

$$\mathbf{Hessian}_{\sigma}(x, y) = \begin{bmatrix} L_{xx}(x, y) & L_{xy}(x, y) \\ L_{xy}(x, y) & L_{yy}(x, y) \end{bmatrix} \quad (1)$$

$$\lambda_{1,2} = \frac{1}{2}(L_{xx} + L_{yy} \pm \sqrt{(L_{xx} - L_{yy})^2 + (2L_{xy})^2}) \quad (2)$$

Hessian matrix was computed by convolving the image with derivatives of the Gaussian kernel, where scale σ represented the standard deviation of the Gaussian kernel and controlled the radius of the detected structures. A coarse fibril mask was produced by computing Hessian matrix and thresholding $\lambda_1(\mathbf{Hessian})$ as below:

$$Mask_{Fibril}(x, y) = \begin{cases} 1 & \lambda_1(\mathbf{Hessian}(x, y)) < \varepsilon \\ 0 & \text{otherwise} \end{cases}$$

Quantification of morphology and spatial organization of fibrils required accurate identification and localization of individual fibrils. Hessian-based detection efficiently segmented regions occupied by fibrils from the background but failed to separate some of the neighboring fibrils and merged them into clusters. To identify individual fibrils a shape analysis and cluster decomposition module is developed as based on previously reported modules.^{91,92} Specifically, first connected component labeling was applied to the detection mask and disconnected blobs were identified. Then, to each detected blob B_i , an ellipse E_i was fitted. Blob and ellipse areas $area(B_i)$, $area(E_i)$, and ratio $r=(area(E_i)-area(B_i))/area(B_i)$ were then computed. Using these size and shape indices, and their means and variances over the image, each detected blob B_i was classified into one of the three classes (spurious detection, single fibril, or fibril cluster). Blobs classified as spurious detection were removed; blobs classified as single fibril were kept intact. Marker-controlled watershed transformation was used to decompose fibril clusters into individual fibrils.⁹³ Regional maxima of distance transform were used as markers. To suppress spurious regional maxima and to prevent over-segmentation, H-maxima transform was applied to the distance transform prior to the detection of regional maxima.⁹⁴

The module then computed parameters related to fibril morphology and spacing, such as fibril radius, fibril area fraction, and interfibrillar distance. From the refined segmentation (Figure 1B), fibril centroids were computed. Delaunay triangulation & vertex coloring were applied to the located centroids, and a colored neighborhood graph was generated, as previously described.^{92,95} In the neighborhood graph (Figure 1C), nodes corresponded to individual fibrils, and edges linked immediate neighbors. For

each node in this neighborhood graph, two specific neighbors were identified, specifically the nearest immediate neighbor (Figure 1D red edges) and farthest immediate neighbor (Figure 1D blue edges). A second graph (nearest/farthest neighborhood graph) was constructed, using only these specific links. Fibril-to-fibril interactions were assessed, and spatial organization of collagen fibrils were described using these two neighborhood graphs. Various descriptors from these graphs such as mean and standard-deviation were then calculated.

Statistical Analysis

Statistical analysis was performed by a biostatistician (RWM). The results of the initial corneal wounds in the pilot dog and the corneal haze scores of all dogs are summarized using descriptive statistics. Clinical scoring, OCT measurements, histopathology scores, picrosirius red measurements and TEM measurements from the other study dogs were analyzed statistically. The mMS scores were analyzed with a two factor ANOVA with treatment being a between-subjects factor and time (day) being a within-subjects (or repeated measures) factor. When evaluating histopathological, immunohistochemistry scores, and picrosirius red measurements between negative controls and alkali-burned corneas, without regards to treatment group, and also between treatment groups, a Wilcoxon rank sum test was utilized. Any difference in the epithelial thickness and total corneal thickness measured in the OCT images between the treatment groups at baseline was detected with a two-sample t-test, while the difference in these measurements between the baseline images and those of alkali-burned corneas was analyzed with a one-sample paired t-test. TEM results were analyzed with a weighted t-test. Weights were used to account for different subsample sizes for the different dogs.

All statistical analyses were performed using standard statistical software SAS v9 (SAS Institute Inc., Cary, NC, USA). All p-values <0.05 were considered statistically significant.

Results

Baseline OCT of Normal Corneas

Prior to performing corneal alkali burn, OCT was performed of both eyes of all dogs to obtain particular measurements. In each OCT image of normal cornea three distinct layers of varying thickness and reflectivity were noted which included (i) the pre-corneal tear film and epithelium, (ii) the stroma and (iii) Descemet's membrane and endothelium. However, for the purposes of this study, only the epithelium and anterior stroma were qualitatively described. The corneal epithelium was poorly reflective and located between the highly reflective pre-corneal tear film and the corneal stroma which demonstrated intermediate reflectivity. The reflectivity of both the epithelium and anterior stroma was primarily homogenous, in part due to the fact that dogs do not have a Bowman's membrane.

The mean epithelial thickness of the right eye and left eye was $77.429 \pm 2.878 \mu\text{m}$ and $78.571 \pm 3.599 \mu\text{m}$, respectively. There was no statistically significant difference in epithelial thickness of the right eyes between treatment groups at baseline ($p=0.82$). The mean total corneal thickness of the right eye and left eye was $545.714 \pm 42.074 \mu\text{m}$ and $555.571 \pm 26.937 \mu\text{m}$, respectively, and there was no statistically significant difference in total corneal thickness of the right eye between treatment groups at baseline ($p= 0.33$).

Corneal Alkali Burn in the Sentinel Dog Supports Development of Fibrosis

The initial mMS scores recorded from the sentinel dog the first day (i.e. day 1) following the alkali burn were 9.5 for the right eye and 10 for the left eye. Ocular health continued to improve throughout the study. Fourteen days after each respective alkali burn, the clinical score of the right eye was 2, which was due to some loss of corneal transparency which occupied 1-25% of the cornea and the clinical score of the left eye was 5.5, which was due to moderate loss of corneal transparency affecting 1-25% of the cornea, mild conjunctival congestion, and a superficial axial corneal ulcer. The corneal haze grade at 14 days post alkali burn was 1 for the right eye and 2 for the left eye.

At the study's endpoint, which was 5 weeks post alkali burn for the right eye and 2 weeks post alkali burn for the left eye, the epithelial thickness of both eyes was variable and the average of four different measurements was $116.75 \pm 28.076 \mu\text{m}$ in the right eye while that of the left eye was $114.25 \pm 22.187 \mu\text{m}$. Total corneal thickness of the right eye was $499 \mu\text{m}$. The left eye's total corneal thickness had increased to $973 \mu\text{m}$. The changes in epithelial thickness and total corneal thickness are highlighted in Table 4. In the anterior corneal stroma of both eyes, an area of increased reflectivity were noted. The foci extended to a depth of $317 \mu\text{m}$ in the right eye and $302 \mu\text{m}$ in the left eye. Additionally, OCT images of the left eye revealed subepithelial foci which were non-reflective, suggestive of corneal edema or bulla formation.

Histopathology of the cornea of the right eye revealed a mildly increased number of stromal nucleated cells in superficial stroma and very small number of inflammatory cells, suggestive of only mild superficial fibrosis. No corneal neovascularization or edema was noted. The scores assigned to the different stains were as followed: Masson's trichrome; 1, EVG: 0, and PAS; 1. Analysis of picosirius red stain revealed a total

collagen area in the wound bed of 34,533 μm^2 . The total area of type I collagen in the wound bed was 31,895 μm^2 (49% of the area corneal tissue measured). The total area of type III collagen in the wound bed was 2,638 μm^2 (4.1% of the area corneal tissue measured). IHC demonstrated mild staining for α -SMA and no staining for CD18.

Histopathological analysis of the left eye's cornea revealed corneal epithelial hyperplasia and fibrosis extending to mid-stroma. Mild corneal neovascularization and marked corneal edema were also noted. The scores assigned to the different stains were as follows: Masson's trichrome; 2, EVG: 2, and PAS: 2. Analysis of picrosirius red stain revealed a total collagen area in the wound bed of 38,663 μm^2 . The total area of type I collagen in the wound bed was 37,430 μm^2 (57% of the area corneal tissue measured). The total area of type III collagen in the wound bed was 1,233 μm^2 (1.9% of the area corneal tissue measured). The section also demonstrated marked staining for α -SMA and no staining for CD18.

Analysis of the TEM images of the burned corneas revealed that the mean area of the collagen fibrils of the right eye was $846.960 \pm 0.0001 \text{ nm}^2$, while that of the left eye was $990.818 \pm 0.0001 \text{ nm}^2$. The mean minimum distance between neighboring collagen fibrils in the right and left eyes was $43.772 \pm 0.000005 \text{ nm}$ and $46.178 \pm 0.000003 \text{ nm}$ respectively. The mean maximum distance between neighboring collagen fibrils was $71.348 \pm 0.000006 \text{ nm}$ for the right eye and $72.5 \pm 4.264 \text{ nm}$ for the left eye. The representative TEM images of the dog corneas are shown in Figure 1.

Alkali Burn is Well Tolerated and Results in Corneal Opacity in 6 additional dogs:

Clinical and Haze Scores

The mMS scores of the dogs were not statistically different between treatment groups at any time point ($p=0.89$), with the highest score (17.5) being recorded for one dog in each treatment group on day 1 (Figure 2A). The mMS scores continued to decrease until the study's endpoint, with an 8 being recorded as the highest score on day 14, while the majority of dogs received a score of 6.5 (Figure 2D). The progression in clinical scores of a representative dog are shown in Figure 2. The exception was a single dog in group A. Over a period of 24 hours, the corneal wound of this dog acutely worsened and was noted to be malacic on day 11. Samples of the cornea were aseptically collected for cytology and culture and sensitivity. The cytology revealed suppurative inflammation with mild epithelial cell atypia. No infectious organisms were appreciated on cytology. Microbes were not detected with culture. All scores from day 11 to day 14 and OCT, histopathological and TEM findings for this particular dog were excluded from analysis.

Significant corneal opacity secondary to alkali burn was appreciated in all dogs at every time point. At the study's endpoint, the mean corneal haze grade was 1.8 ± 0.447 . The formation of corneal haze is demonstrated in Figure 2D.

OCT Findings Support Development of Corneal Fibrosis

The OCT images at the study's endpoint demonstrated several pathologic changes all dogs' right corneas. The reflectivity of the epithelium had increased and the thickness was variable. Images revealed foci of a hyper-intense signal in the anterior stroma. Additionally, some images contained foci within the epithelium that were non-reflective, suggestive of bulla formation. These changes were confined to the axial cornea and did not differ between treatment groups.

Following the alkali burn, the mean epithelial thickness of the six dogs' right eyes was $83.9 \pm 23.213 \mu\text{m}$, and the mean total corneal thickness was $906.8 \pm 148.417 \mu\text{m}$. The mean epithelial thickness following the alkali burn did not differ significantly from the baseline epithelial thickness, irrespective of treatment ($p=0.5334$), indicating that alkali-burned corneas re-epithelized, typical of normal corneal wound healing. The mean epithelial thickness of group A was $86.75 \pm 20.860 \mu\text{m}$, while that of group B was $82.0 \pm 25.158 \mu\text{m}$. The mean total corneal thickness of all dogs, regardless of treatment group, was statistically greater than that of the baseline images ($p=0.004$). The mean total corneal thickness of group A was $793.50 \pm 212.839 \mu\text{m}$, while that of group B was $982.333 \pm 3.215 \mu\text{m}$. The measurements for individual dogs are provided in Table 4. There was no statistical difference between treatment groups regarding epithelial thickness or total corneal thickness ($p=0.837$, $p=0.302$, respectively). These changes detected with OCT are highlighted in Figure 3 as representative OCT images of alkali-burned corneas (Figure 3B and 3C) demonstrated notable increased epithelial and total corneal thickness compared to normal cornea at baseline (Figure 3A).

Fibrotic Changes Appreciated on Histopathology

Various histopathological corneal changes were noted on H&E slides of the alkali-burned corneas and included: mild corneal epithelial hyperplasia, presence of fibrin, a few lymphocytes and neutrophils and many fibrocytic cells in stroma, mild erosion of epithelium and focal absence, thickening, disorganization and destruction of epithelial basement membrane (Figure 4E). Varying degrees of edema and neovascularization formation were noted in all alkali-burned corneas, except for one dog receiving Treatment A who did not appear to develop corneal neovascularization. There

was no significant difference between alkali-burned corneas and negative controls when comparing severity of corneal neovascularization or edema ($p=0.107$), and a significant difference in corneal neovascularization or edema formation was not detected between treatment groups ($p=0.3$). The grades for corneal edema and neovascularization are shown in Table 5.

It was grossly apparent that the staining pattern for Masson's trichrome, EVG and PAS stains differed between the negative control and alkali-burned corneas and scores for each stain are displayed in Table 5. The epithelium and anterior stroma of the negative control corneas stained in a homogenous. The epithelium following Masson's trichrome staining appeared red while the stromal collagen fibers stained blue (Figure 4B). Following EVG staining, the epithelium was a dark purple-black color while the stroma stained fuchsia (Figure 4C). Finally, the PAS stained negative control corneas included a light purple epithelium and light pink stroma (Figure 4D). Following the alkali burn, an increased number of spindle fibrocytic cells were noted in the anterior stroma of the Masson's trichrome stained corneas as evidenced by the increased red stain in this area (Figure 4F). The EVG stained alkali-burned corneas showed increased dark purple-black staining in the anterior stroma, suggestive of elastic fiber deposition (Figure 4G). Finally, PAS stained alkali-burned corneas had an increase in dark pink-purple staining in the anterior stroma, suggestive of increased fibrin deposits and/or increased basement membrane formation (Figure 4H). Despite these visually obvious differences between negative control and alkali-burned corneas, no significant difference was detected in this small sample size (Masson's trichrome, $p=0.125$, EVG, $p=0.143$; PAS,

p=0.143). Similarly, there was no significant difference between treatment groups with regards to the degree of staining (Masson's trichrome, p=0.6; EVG, p=0.4; PAS, p=0.5).

There was a marked, visible contrast between negative control and alkali-burned corneas with picrosirius red staining, as shown in Figure 5. Negative control corneas were primarily comprised of red-yellow-orange fibers with very few green fibers noted, demonstrating the predominance of type I collagen in normal cornea and these fibers were also arranged in a precise, parallel manner (Figure 5A). Alkali burned-corneas demonstrated an increased amount of green fibers, indicating an upregulation of type III collagen compared to negative controls. The collagen fibers in the alkali-burned corneas were notably disorganized (Figure 5B). The areas of type I collagen, type III collagen, and total collagen of the control dogs and study dogs were also quantified and these values are displayed in Table 6. Although grossly obvious, the marked increase in type III collagen in the alkali-burned corneas only approached significance (p=0.071). There was no statistical difference in area of type I collagen or total collagen between negative control and alkali-burned corneas (p=0.25, p=0.25, respectively). A significant difference was not detected between treatment groups in regards to type I collagen area (p=0.8), type III collagen area (p=0.2) or total collagen area (p=1.0)

Presence of α -SMA Indicates Cellular Transdifferentiation

To determine the cell types present in the anterior stroma, immunohistochemistry was performed, specifically antibodies against α -SMA were used to identify fibroblasts, while leukocytes were stained with antibodies against CD18. Grades for these IHC stains are provided in Table 5. Negative control corneas did not stain positively for α -SMA or CD18, while alkali-burned corneas demonstrated marked α -SMA staining and no-

moderate staining for CD18 (Figure 6B). The increase in α -SMA staining in the alkali-burned corneas was significant when compared to negative control corneas ($p=0.018$). The faint staining for CD18 in the alkali-burned corneas was not significant ($p=0.143$). A significant difference between treatment groups was not detected with regards to the degree of α -SMA or CD18 staining ($p=0.4$ for both IHC).

Transmission Electron Microscopy Reveals Disorganization of Collagen Fibrils

Ultrastructural analysis of the corneas was utilized for analysis of stromal collagen fibril arrangement (Figure 7). Marked stromal collagen fibril disorganization, characteristic of fibrosis, was detected. Mean values of these parameters measured in control and experimental corneas are shown in Table 7. No statistical difference was noted in the area of ($p= 0.108$), and minimum ($p= 0.26$) and maximum ($p=0.205$) distances between collagen fibrils between left eyes of study dogs and control dogs, demonstrating that there was no breed related differences in these parameters. When comparing the study dogs, regardless of treatment group to control dogs, both the minimum and maximum distances between collagen fibrils was significantly greater for the dogs that underwent the alkali burn ($p=0.026$, $p=0.018$, respectively) as demonstrated in Figure 7B. When comparing the two treatment groups to each other, there was no statistical difference in the mean area of collagen fibrils ($p=0.822$), the mean minimum distance between collagen fibrils ($p=0.445$) or the maximum distance between collagen fibrils ($p=0.404$).

Discussion

Current *in vivo* models of corneal fibrosis possess several limitations. The corneal anatomy of the animals commonly utilized in ophthalmic research differs

significantly from that of people. For example, the mouse central corneal thickness ranges from 0.089-0.123 mm, the rat is 0.16 mm, and a rabbit has a central corneal thickness of 0.36 mm. By contrast, the central corneal thickness in people has been reported as 0.54 mm. The dog's central corneal thickness of 0.5-0.66 mm is more similar to people.⁶² Using the dog as an animal model, the responses to corneal injury and to experimental therapies are likely to be more representative of the possible responses seen in people and is therefore deemed more appropriate.

In addition to thin corneas, mice and rats have corneas that are quite small in diameter compared to people (approximately 2 mm versus 11 mm respectively).^{96,97} Due to their small diameter it can be difficult to isolate the axial cornea when performing an alkali burn. Induced chemical injury typically extends to the limbus resulting in a depletion of corneal limbal stem-cells. In fact, the alkali burn is commonly used to induce limbal stem-cell deficiency (LSCD) in an experimental setting⁹⁸ to study LSCD in people, a common sequela to chemical injury.⁹⁹⁻¹⁰¹ As a consequence of LSCD, corneal repair mechanisms are significantly altered, resulting in persistent ulceration, neovascularization and loss of transparency.^{102,103} Consequently, if a corneal alkali burn model is used to assess therapies for corneal fibrosis that do not involve LSCD, the assessment of the wound healing response and the efficacy of investigative therapies may be inaccurate if rats or mice are used due to the high likelihood of limbal damage in these small species.

To better address these concerns in currently utilized animal models of corneal disease, our group has developed a new animal model of corneal fibrosis. In previous studies corneal fibrosis has been generated *in vivo* with photorefractive keratectomy

(PRK), repeated epithelial abrasions, penetrating keratectomy, laceration and suture placement, sulfur mustard exposure and an alkali burn. Photorefractive keratectomy requires specialized equipment, specifically an excimer laser. Those performing the PRK must undergo extensive training to successfully create corneal fibrosis and the resulting corneal scars can be subtle.⁵⁶ Similarly, the corneal haze caused by repeated debridement of the canine cornea by Bentley group was indistinct.¹⁰⁴ Previous studies have demonstrated that rodents and rabbits can tolerate a small (1 mm or less) penetrating keratectomy.¹⁰⁵ In contrast, full thickness corneal wounds in dogs can result in significant anterior uveitis and iris prolapse.¹⁰⁶ Thus, this technique was inappropriate for this translation study. Additionally, the use of a linear laceration and suture placement⁶⁶ was excluded as the presence of suture in the cornea was considered a possible confounding factor to the corneal wound healing process and an additional irritant to the dogs. Exposure to sulfur mustard can generate notable corneal fibrosis. However, this chemical is a select agent and is known to cause serious injuries to other organ systems and cannot be used in normal laboratory setting due to the risk to those performing the procedure.¹⁰⁷ Thus, the alkali burn represented the ideal method to produce corneal fibrosis as it does not require specialized training or expensive equipment, is safe to those carefully handling the NaOH solution, does not require special laboratory setting and creates a visible corneal scar.

The present study demonstrated that the corneal alkali burn was well-tolerated by dogs, as their mMS scores continued to improve throughout the study. Only one dog was excluded from the study as the right eye developed keratomalacia. Thorough diagnostic testing, including cytology and culture, did not reveal any infectious agents. Due to the

acute presentation and rapid progression of keratomalacia coupled with failure to detect any pathogens, it was suspected that the cornea of this dog experienced a traumatic event. Each dog was caged with one other dog for socialization purposes, and although the dogs tolerated their cage mate throughout the study, it is possible that this particular dog's cage mate scratched or excessively licked her affected eye. The progression of the corneal wound was deemed unrelated to the initial alkali burn, and it was appropriate to exclude this dog's clinical scores from day 11 to day 14 and also all OCT, histopathological, and TEM findings from final analysis.

The alkali burn generated significant fibrotic changes in the dog cornea. The degree of fibrotic change appeared to depend on the duration of alkali burn, as the cornea haze grade, histopathology and IHC scores were lower in the sentinel dog's right eye (15 second burn) than the left (30 second burn). The sentinel dog's corneal findings consisted of a small amount of corneal haze in the right eye and bulla formation in the left, and so we determined that optimal alkali burn time in this pilot project to be 20 seconds and this duration of alkali burn was used for all remaining study dogs.

A 20 second alkali burn was able to generate marked corneal haze and resulted in abnormalities on histopathology and IHC suggestive of fibrosis. H&E sections of the affected corneas revealed that the cellularity of the superficial stroma was markedly increased. Although a minority of these stromal cells stained positively for CD18, suggesting an inflammatory lineage, it appeared that the majority of cells stained positively for α -SMA, a known hallmark of fibrosis.^{58,108} This staining for α -SMA was significantly increased in the alkali-burned corneas when compared to control corneas, thereby suggesting that the alkali burn induced the transdifferentiation of corneal

fibroblasts to myofibroblasts. Importantly, histopathology of affected corneas in this study did not reveal changes secondary to LSCD.^{101,109,110} The alkali burn protocol developed in the current study reliably created axial corneal fibrosis while preserving the limbal stem-cells.

The results of special stains, specifically Masson's trichrome and picrosirius red, confirmed development of corneal fibrosis following the alkali burn. The corneal stroma contains collagen types I, III, IV, V and VI.¹¹¹⁻¹¹⁴ The different collagens are assembled into banded fibrils, arranged in an orthogonal manner within the corneal stroma. This precise organization of corneal fibrils, in addition to the fixed quantity of each collagen type, allows for minimal light scattering and subsequent transparency.¹¹⁵ With the disruption of this arrangement or deposition of excess collagen of any type, corneal transparency is lost, replaced by fibrosis. Masson's trichrome stain and picrosirius red stain have been utilized to detect collagen fibers in other organ systems including the heart, kidneys and liver, and increased quantity of these stains signifies fibrosis.¹¹⁶⁻¹¹⁹ However, unlike the cornea, these other organs do not contain significant collagen. Therefore, in the current study, the Masson's trichrome and picrosirius red stains had to be evaluated and scored to accommodate the cornea's native collagen content. For Masson's trichrome stained corneas the increased red staining in the anterior stroma represented mesenchymal cells, either fibroblast or vascular endothelial cells.¹²⁰ Cell type was verified with α -SMA, confirming that the predominant cell population was composed of fibroblasts. The picrosirius red stain not only demonstrated transitions in collagen type but also in collagen fibril arrangement. It has been well established that the proportion of different corneal collagen types changes significantly during the process of

fibrosis, as type I collagen which predominates in normal cornea is replaced by type III collagen in a corneal scar.^{26,121} Analysis of the picrosirius red stain in our study showed a significant increase in type III collagen in the alkali-burned corneas compared to negative controls corneas. Finally, collagen fibrils appeared extremely disorganized with the picrosirius red stain between negative control and alkali-burned corneas supportive of collagen remodeling typical of fibrosis.

The results of the EVG stain further supported the development of corneal fibrosis following the alkali burn. EVG is used to identify elastic fibers.¹²² Reports of elastic fibers in the mammalian cornea are sparse and conflicting,¹²³⁻¹²⁵ and to our knowledge elastic fibers have not been detected in the axial cornea of dogs. In other organ systems, which contain some elastic fibers normally, such as the lung, the presence and proportion of elastic fibers can determine the degree of fibrosis.¹²⁶ Consequently, the increased quantity of this stain in the anterior stroma of the alkali-burned corneas further supports fibrotic change in this novel model.

Structural analysis of the corneas with OCT complemented histopathology findings. The corneal epithelium was variably thickened, consistent with epithelial hyperplasia, and the foci of hyper-intense signal in the anterior stroma likely represented the increased cellularity noted on histopathology. OCT is routinely used in physician ophthalmology and allows for non-contact, non-invasive imaging that assists in the diagnosis and management of several corneal diseases, including ocular surface squamous neoplasia, corneal epithelial basement membrane dystrophy, keratoconus and bullous keratopathy.¹²⁷⁻¹³⁰ People with corneal scarring associated with an irregular Bowman's membrane undergo OCT imaging prior to phototherapeutic keratectomy

(PTK) to measure the depth of their corneal scars and allow for surgical planning. A corneal scar on these OCT images is defined as (1) an area of cornea that demonstrates a hyper-intense signal that corresponds with scarring noted on clinical examination and (2) an area of cornea with variable epithelial thickness by a minimum of 33% from the baseline epithelial thickness.¹³¹ In the current study, the maximum increase in corneal epithelial thickness was 75.3%. Study dogs demonstrated hyper-intense signals within the anterior stroma of the burned area. Our OCT findings, coupled with our clinical examination findings, support the conclusion that this study protocol effectively creates corneal fibrosis in dogs similar to that described in physician ophthalmology.

Transmission electron microscopy allows for ultrastructural analysis of both normal and pathologic tissue architecture. The size of and distance between collagen fibrils in normal human cornea has been reported, and these measurements appear to be dependent on the methods of fixation and embedding resin used during processing.¹³² Documented collagen fibril diameter and interfibrillar spacing ranges from 25-35 nm and 38.0-52.5 nm, respectively.¹³²⁻¹³⁴ To our knowledge, the distance between collagen fibrils in the normal canine cornea has not yet been established, while the collagen fibril diameter for normal corneas of the Beagle has been previously reported as 28.3 ± 3.49 nm.¹³⁵ Investigations of these parameters in normal corneas of other dogs breeds remains non-existent. Here, it was found that the average size and spacing of the collagen fibrils did not differ from that of normal Beagle stroma in the dog breeds which served as controls (Poodle, American Pit bull terrier and mixed breed dog). Although the sample population for this analysis was small, this ultrastructural analysis represents the first comparison of corneal collagen fibril organization among different breeds. Differences

in other anatomical aspects of the cornea such as nerve fiber density have been detected among different dog breeds, dependent on skull type;¹³⁶ it may, therefore, be of interest to pursue additional studies aimed at comparing collagen fibril size and spacing among different cat and dog breeds utilizing a larger sample population. Despite the lack of published normal values for collagen fibril size and organization in dog cornea, a significant difference in the minimum and maximum interfibrillar distance was detected between normal and wounded corneas in this study. This increase in spacing and subsequent disorganization of corneal collagen fibrils has been previously documented in other studies evaluating corneal scars in people and laboratory animals thereby indicating that the alkali burn is able to generate corneal fibrosis.^{133,137,138} As previously mentioned, the use of TEM is sparse in studies evaluating dog corneas, regardless of pathology. We quantified corneal fibril changes noted on TEM using advanced computer modeling via a multi-scale Hessian matrix system. This current study represents pioneering research, demonstrating the value of computer analysis of TEM images as an objective, yet highly specific means by which corneal fibrosis in dogs can be quantified in the research setting.

Interestingly, there did not appear to be difference in the degree of fibrosis between the treatment groups. Our laboratory has previously established that SAHA prevents corneal fibrosis. Specifically, Bosiak *et. al.* and Donnelly *et. al.* demonstrated that SAHA prevents TGF- β 1 mediated canine and equine corneal fibrosis *in vitro* and Tandon *et. al.* found that SAHA reduced corneal haze in rabbits following PRK.⁵⁷⁻⁵⁹ While the efficacy of SAHA as an anti-fibrotic has been repeatedly demonstrated, the molecular mechanisms by which it inhibits fibrosis in the cornea have not been extensively investigated in the current literature. Consequently our laboratory has sought

to determine the mechanisms of action of SAHA as a corneal anti-fibrotic agent. Recent research by our laboratory has shown that SAHA inhibits corneal fibrosis by modulating both canonical (Smad) and non-canonical (ERK1/2) components of TGF- β 1 intracellular signaling pathways and also matrix metalloproteinase 2 and 9 activity (Gronkiewicz, unpublished data). In another recent study, which did not specifically evaluate the anti-fibrotic effects of SAHA, the various molecular mechanisms by which SAHA inhibits corneal neovascularization were determined. Here, SAHA prevented corneal neovascularization by attenuating hemangiogenesis, inflammatory pathways and lymphangiogenesis.⁶⁹

Failure to detect a statistically significant difference between treatment groups may be due to the relatively small number of dogs examined in this study. The minimal number of animals deemed necessary to detect a difference between treatment and control dogs was utilized in accordance to institutional animal care and use guidelines. Six dogs were deemed appropriate after careful review of other studies which included sample sizes of 6 or less animals.¹³⁹⁻¹⁴¹ Despite support from the literature, our small sample size increased the probability of type II error. With type II error, the null hypothesis of the study is accepted, when in fact it is false. Thus, there may have been a significant difference in the severity of fibrosis between the treatment groups. Another possible reason that the two treatment groups did not differ was the potential ineffective dosage of SAHA used in the current study. Previous studies performed by our laboratory determined that SAHA at a concentration of 25 μ M was able to reduce corneal haze following PRK in rabbits.⁵⁹ However, that particular study design differed significantly in terms of the laboratory animal utilized and the methodology utilized to create corneal

fibrosis. The alkali burn in the canine cornea creates more significant inflammation and fibrosis than PRK in the rabbit cornea. Therefore, it is possible that the concentration of SAHA needed to prevent fibrosis secondary a corneal alkali burn is greater than 50 μM . Additional studies with larger sample size and different doses are warranted to better investigate the efficacy of SAHA as an anti-fibrotic *in vivo*.

Conclusion

The canine corneal alkali burn described here is well tolerated and does not damage the corneal limbus. The development of fibrosis was confirmed by histopathology, IHC, OCT and TEM. Treatment with SAHA did not appear to reduce severity of fibrosis in this pilot study.

APPENDIX 1: TABLES

Table 1. Sequences of primers for detecting MMP RNA

MMP	Primer	Sequence	Source
MMP1	Forward	5'GGGTCATTCTCTTGGACTTTCT3'	Canine
	Reverse	5'AGCTGGACATTGCCACTATAC3'	Canine
MMP2	Forward	5'CTGACCAAGGGTACAGCTTATT3	Canine
	Reverse	5'CAGACGGAAGTTCTTGGTGTAG3'	Canine
MMP8	Forward	5'CCACACTCCGTGGAGAAATAC3	Canine
	Reverse	5'GGATGGCCAGAACAGAGAAA3'	Canine
MMP9	Forward	5'CTACGACCAGGACAAACTCTAC3'	Canine
	Reverse	5'TTGCCCAGGAAGATGAAGG3'	Canine

Table 2. Tissue targets of special histopathology stains

Stain	Target	Result Scored
Masson's Trichrome	Mesenchymal cells	Red stain
Elastica van Gieson	Elastic fibers	Black stain
Periodic acid-Schiff	Basement membrane and fibrin	Dark pink-light purple

Table 3. Scoring system for severity of corneal neovascularization, edema and stain

Score	Severity of neovascularization, edema or staining
0	No neovascularization, edema or staining noted
1	Mild neovascularization, edema or staining
2	Moderate neovascularization, edema or staining
3	Marked neovascularization, edema or staining noted

Table 4. Possible orientation patterns based on the value of eigenvalues λ_1, λ_2 of the Hessian matrix ($|\lambda_1| \geq |\lambda_2|$)¹⁴²

λ_1	λ_2	Orientation Pattern
Low	Low	Flat or Noise no preferred direction
High -	Low	Bright tubular structure
High +	Low	Dark tubular structure
High -	High -	Bright blob-like structure
High +	High +	Dark blob-like structure

Table 5. Epithelial and total corneal thickness measurements at baseline and following the alkali burn. Multiple measurements of epithelium performed after alkali burn are expressed as a mean.

Dog	Baseline Epithelial Thickness (μm)	Baseline Total Corneal Thickness (μm)	Post Burn Epithelial Thickness (μm)	Post Burn Total Corneal Thickness (μm)
Sentinel Dog OD	80	600	116.75	499
Sentinel Dog OS	80	576	114.25	973
Dog 1 (A)	79	498	101.5	643
Dog 2 (A)	76	582	72	944
Dog 4 (B)	78	530	60.25	986
Dog 5 (B)	73	506	107.5	981
Dog 6 B)	81	519	107.5	980

Table 6. Scores for severity of corneal neovascularization, corneal edema and special stains

Dog	CNV	Edema	MT	EVG	PAS	α -SMA	CD-18
Rep.control dog	0	0	0	0	0	0	0
Dog 1 (A)	0	0	0	0	0	2	0
Dog 2 (A)	2	1	2	3	2	3	2
Dog 4 (B)	2	3	2	3	2	3	2
Dog 5 (B)	3	1	3	3	1	3	2
Dog 6 (B)	3	3	2	3	3	3	2

Table 7. Area of type I collagen, type III collagen and total collagen in the wound bed (alkali-burned corneas) and axial cornea (control cornea)

Dog	Area of Type I Collagen (μm^2)	Area of Type III Collagen (μm^2)	Area of Total Collagen (μm^2)
Control dog	35887	1136	37023
Control dog	38446	385	38831
Control dog	39563	618	40181
Dog 1 (A)	41526	1539	43065
Dog 2 (A)	5083	763	5846
Dog 4 (B)	21329	15531	36860
Dog 5 (B)	22345	1725	24070
Dog 6 (B)	4673	5382	10055

Table 8. Corneal collagen fibril dimensions measured with TEM

Group	Collagen Fibril Area (nm^2)	Minimum Interfibrillar Distance (nm)	Maximum Interfibrillar Distance (nm)
Control Dogs (n= 3)	763.428 \pm 0.00005	42.960 \pm 2.680	70.144 \pm 5.427
Beagles: Left Eye (n= 7)	877.309 \pm 168.889	45.377 \pm 4.777	74.410 \pm 7.9
Beagles: Alkali-burned (n= 5)	845.558 \pm 113.119	47.829 \pm 3.304	92.621 \pm 14.774
Beagles: Treatment A (n= 2)	835.304 \pm 85.467	46.58 \pm 3.022	86.372 \pm 3.426
Beagles: Treatment B (n= 3)	852.394 \pm 131.628	48.66 \pm 3.34	96.787 \pm 17.951

APPENDIX 2: FIGURES

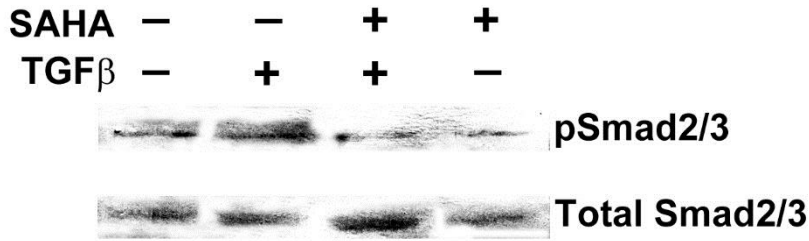


Figure 1. Representative western blot showing the effect of SAHA +/- TGF-β1 on Smad phosphorylation in canine corneal fibroblast (CCF) cell extracts. TGF-β1 treatment of CCF caused a 2.8 ± 0.28 fold ($p < 0.01$) increase in Smad2/3 phosphorylation. SAHA treatment of CCF significantly ($p < 0.01$) attenuated TGF-β1-induced Smad2/3 phosphorylation.

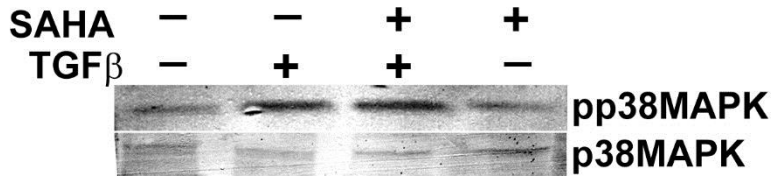


Figure 2. Representative western blot showing the effect of SAHA +/- TGF-β1 on p38 mitogen-activated protein (MAP) kinase phosphorylation in canine corneal fibroblast (CCF) cell extracts. TGF-β1 treatment of CCF caused a 3.5 ± 0.66 fold ($p < 0.05$) increase in p38 MAP kinase phosphorylation. SAHA treatment of CCF did not significantly attenuate TGF-β1-induced p38 MAPK phosphorylation.

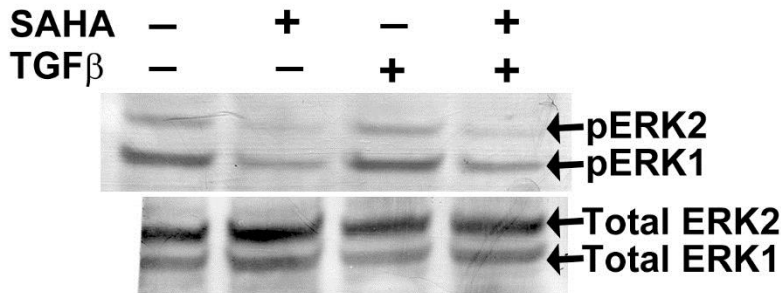


Figure 3. Representative western blot showing the effect of SAHA +/- TGF-β1 on ERK1 and ERK2 phosphorylation in canine corneal fibroblast (CCF) cell extracts. TGF-β1 alone did not modulate the phosphorylation of ERK1 or ERK2, while exposure to SAHA with or without the concurrent TGF-β1 treatment resulted in significantly reduced expression of p-ERK1 (2.7 ± 0.6 fold decrease, $p < 0.01$) and p-ERK2 (8 ± 3 fold decrease,

p<0.05) which suggests that SAHA treatment inhibited ERK phosphorylation, regardless of TGF- β 1 activity.

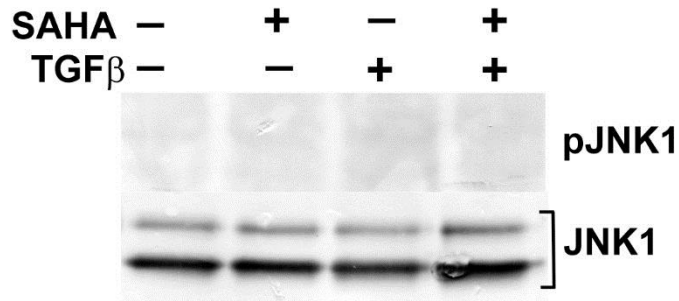


Figure 4. Representative western blot showing the effect of SAHA +/- TGF- β 1 on JNK phosphorylation in canine corneal fibroblast (CCF) cell extracts. As can be seen in the western blot, no p-JNK1 was detected in the untreated control CCF. Neither TGF- β 1 nor SAHA alone or in combination showed any effect on p-JNK1 expression.

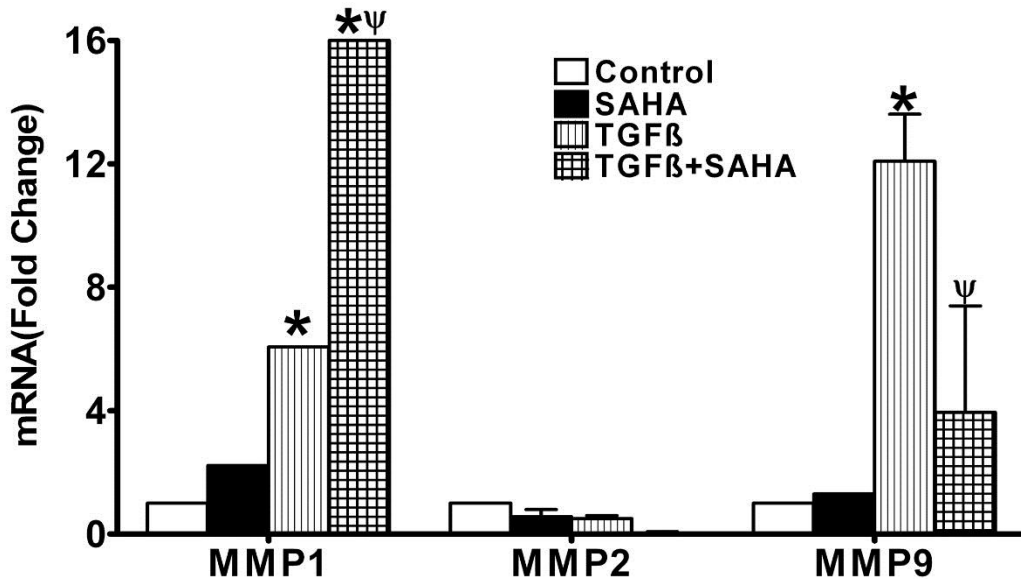


Figure 5. Graph showing real time qPCR mRNA quantification of matrix metalloproteinases (MMPs) 1, -2 and -9 in canine corneal fibroblasts (CCF). TGF- β 1 treatment of CCF caused a 6 fold (p<0.01) increase in MMP1 mRNA and 10 fold (p<0.01) increase in MMP9 mRNA expression and did not cause any notable change in MMP2 mRNA. SAHA treatment of CCF alone did not cause any notable change in MMP1, MMP2 or MMP9 expression but concurrent treatment of CCF with TGF- β 1 caused a significant increase (p<0.05) in MMP1 mRNA and a significant decrease (p<0.05) in the MMP9 mRNA expression.

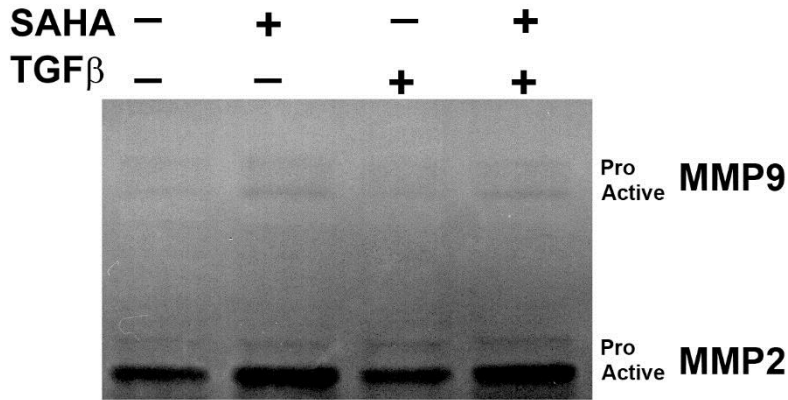


Figure 6. Representative gelatin zymography demonstrating the effect of SAHA +/- TGF- β 1 on MMP2 and MMP9 protein expression in canine corneal fibroblast (CCF) cell extracts. MMP2 and MMP9 proteins were detected in untreated control CCF, and treatment with TGF- β 1 alone did not alter this baseline MMP protein expression. However, treatment with SAHA, irrespective of co-treatment with TGF- β 1 resulted in a statistically significant increase in MMP2 and MMP9 protein expression.

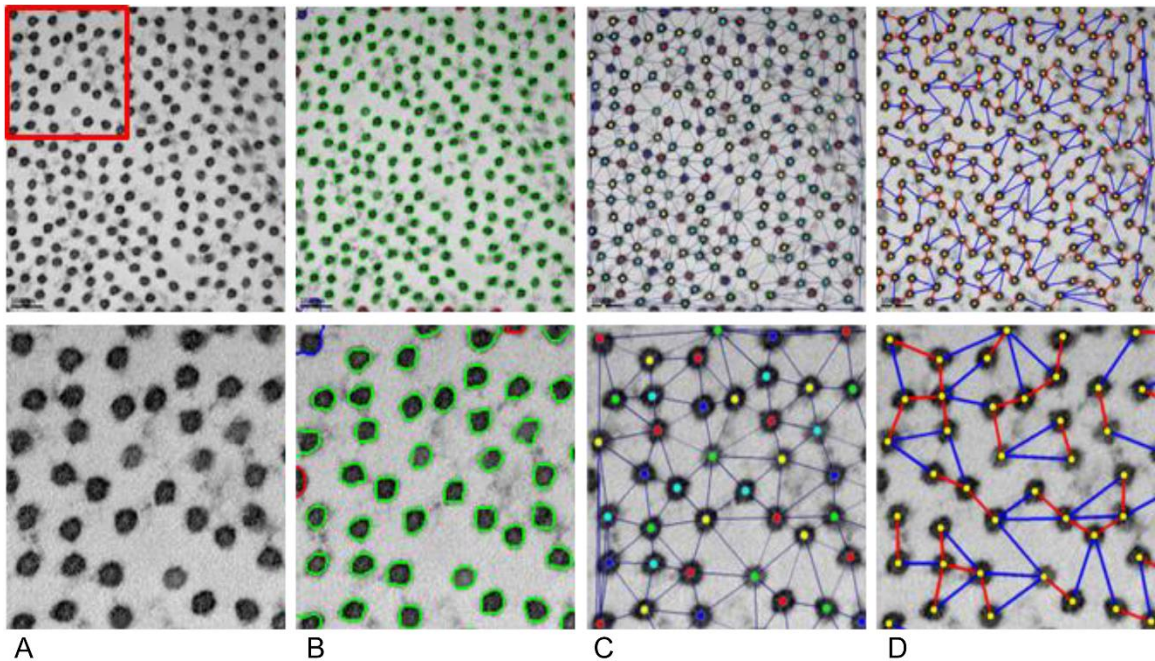


Figure 7. Image analysis and quantification for TEM images of collagen fibril cross-sections. First row: original image at 25,000X magnification; second row: magnified region. A) Original TEM image. B) Collagen fibril segmentation results. C) Fibril centroids and fibril neighborhood graph. D) Nearest (red) and farthest (blue) immediate neighbors.

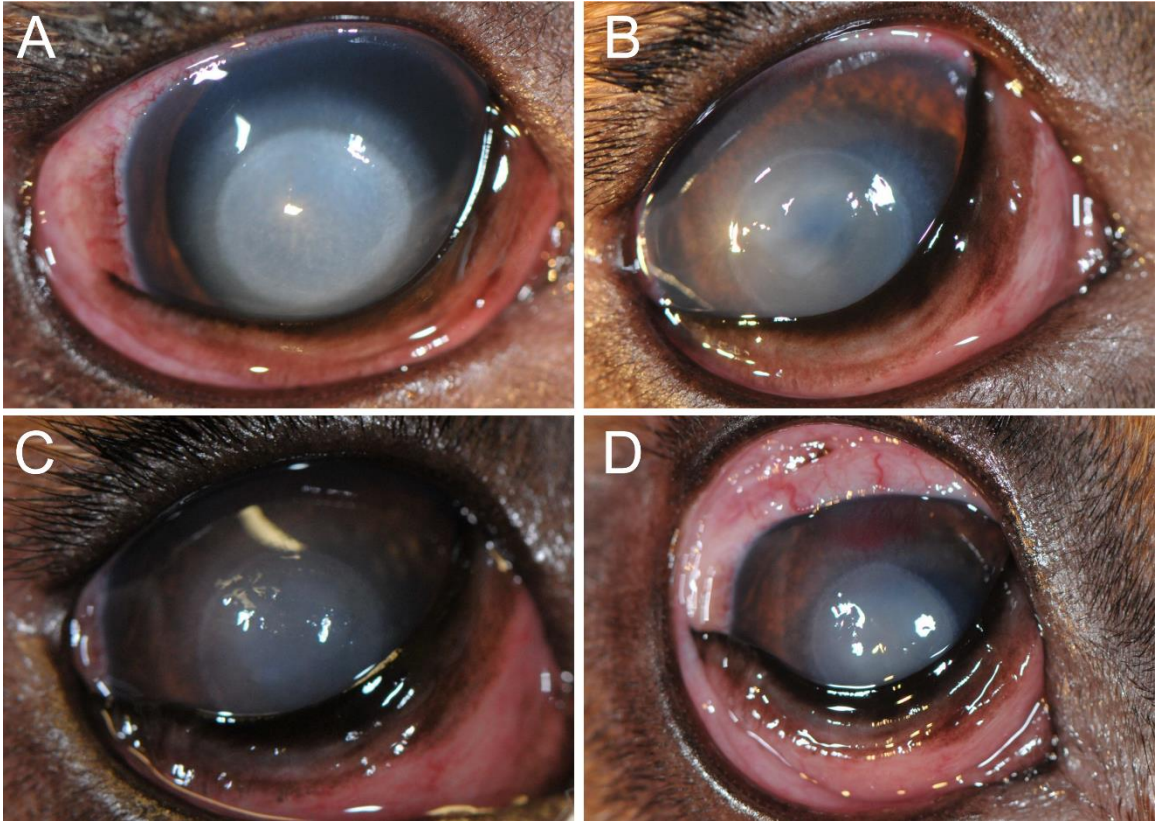


Figure 8. Clinical scores and corneal haze grades following the 20 second alkali burn in a representative dog. A) One day following alkali burn, the mMS score was 17.5 and corneal haze grade was 3. B) On day 5 the mMS score was 11 and corneal haze grade was 2. C) Ten days post-alkali burn the mMS score was 8.5 and corneal haze grade was 2. D) At the study's endpoint (day 14), the mMS score was 6.5 and corneal haze grade was 2.

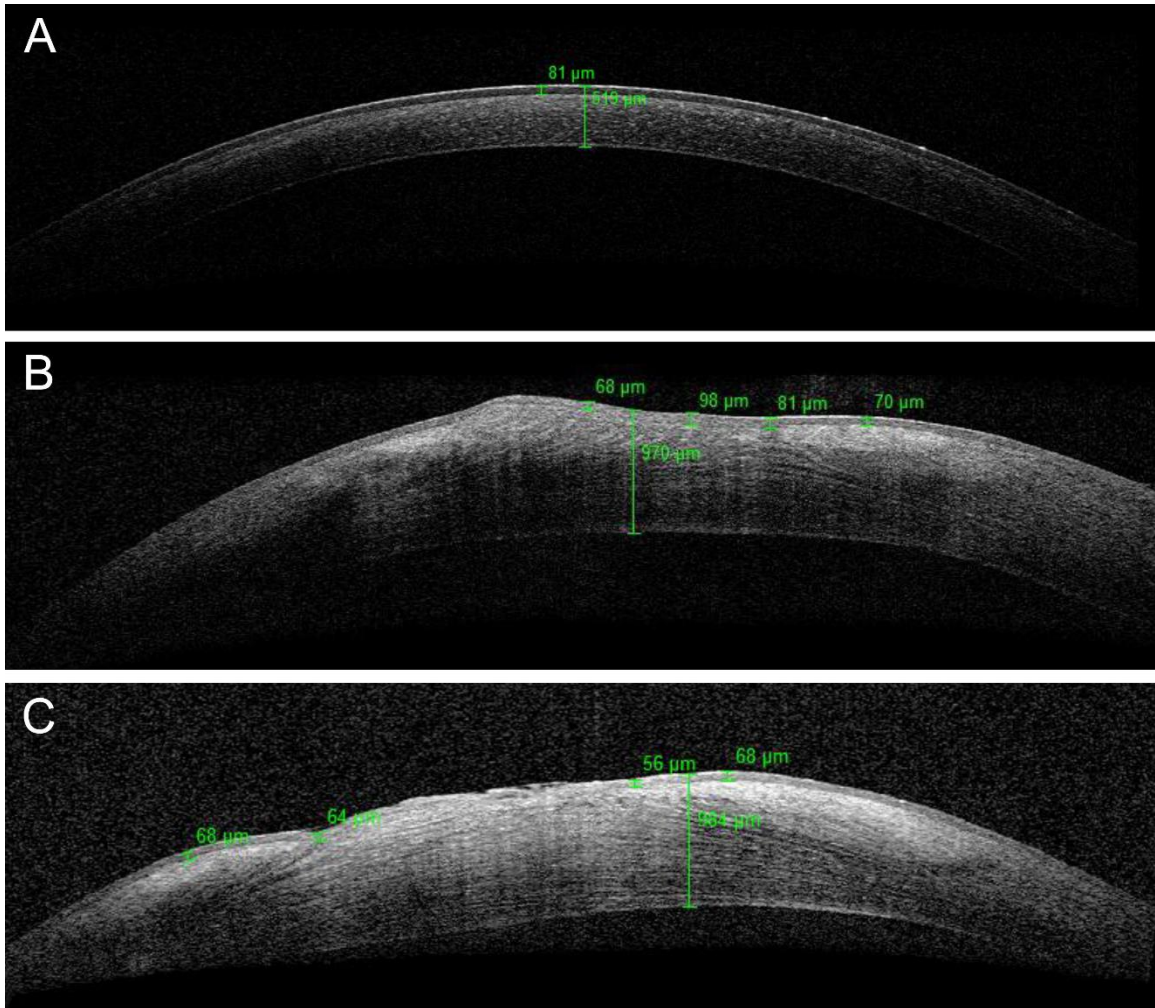


Figure 9. Representative OCT images of normal cornea at baseline and alkali-burned cornea 14 days after wounding. A) Normal cornea of a dog prior to wounding. The values in green represent epithelial and total corneal thickness. B) Alkali-burned cornea from dog in treatment group A. C) Alkali-burned cornea from dog in treatment group B. Note the variable epithelial thickness and the increased total corneal thickness in the alkali-burned cornea compared to the normal cornea at baseline.

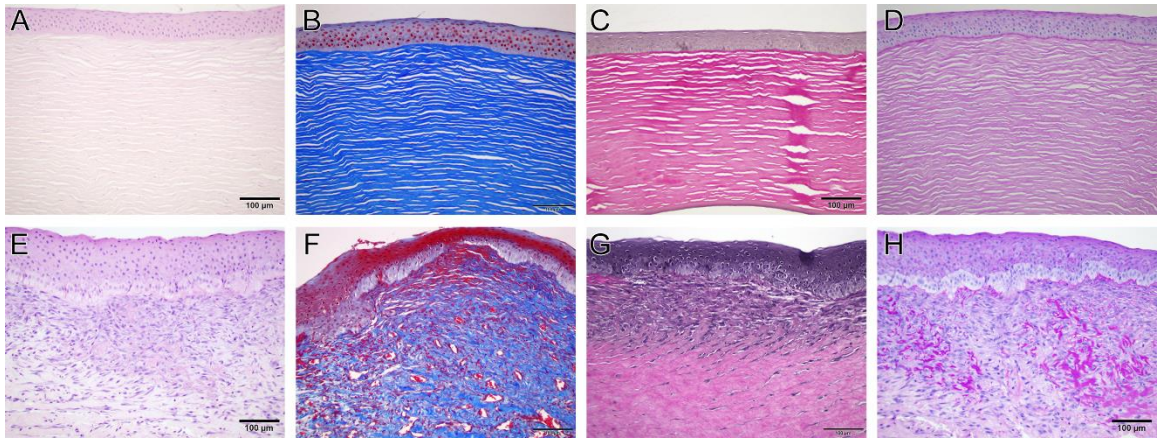


Figure 10. Representative histological images of normal (A-D) and alkali-burned corneas (E-H). H&E stain demonstrated an increased cellularity of the anterior stroma in the alkali-burned corneas (E) compared to normal corneas (A). Masson's trichrome stain of the alkali-burned cornea (F) confirmed presence of mesenchymal cells in the anterior stroma, which are absent in normal cornea (B). The formation of elastic fibers was demonstrated in the alkali-burned cornea with EVG (G). No elastic fibers were detected in normal cornea (C). PAS stained corneas showed increased basement membrane and fibrin deposition in the alkali-burned cornea (H) compared to normal cornea (D).

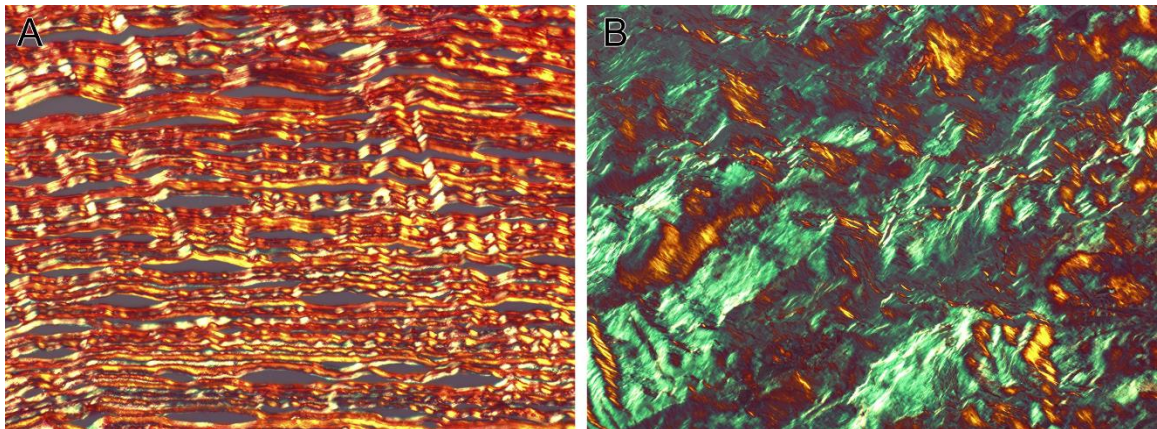


Figure 11. Representative Picrosirius red stained negative control (A) and alkali-burned (B) corneas. Note the increased amount of type III collagen fibers in the alkali-burned cornea compared to the negative control. This transition of type I to type III collagen fibers is typical of scar formation.

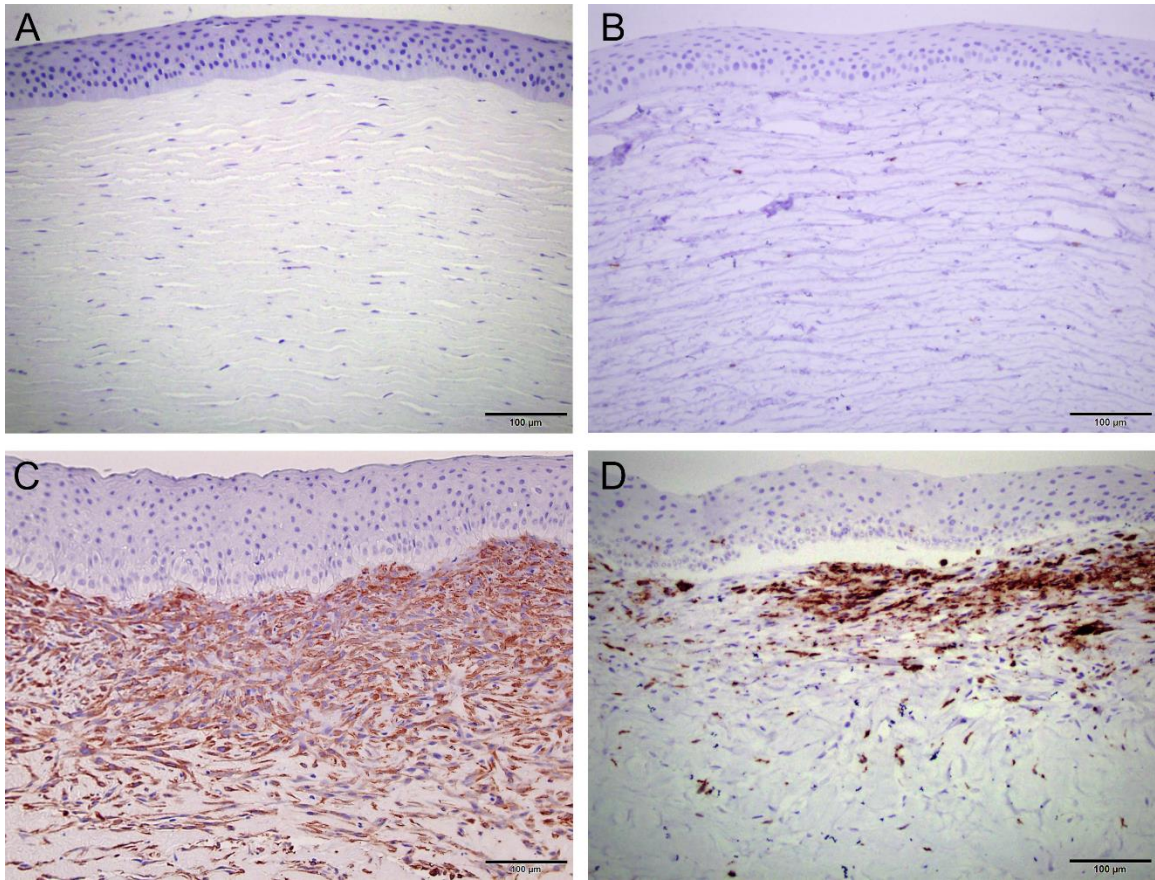


Figure 12. Representative immunohistochemistry of normal (A) and alkali-burned (B) corneas. Increased α -smooth muscle actin stain in the alkali-burned corneas confirmed the cell population in the anterior stroma as fibroblasts. There was only a mild-moderate increase in CD18 stain in the alkali-burned cornea indicating that the majority of the cellular infiltrate was not inflammatory in nature.

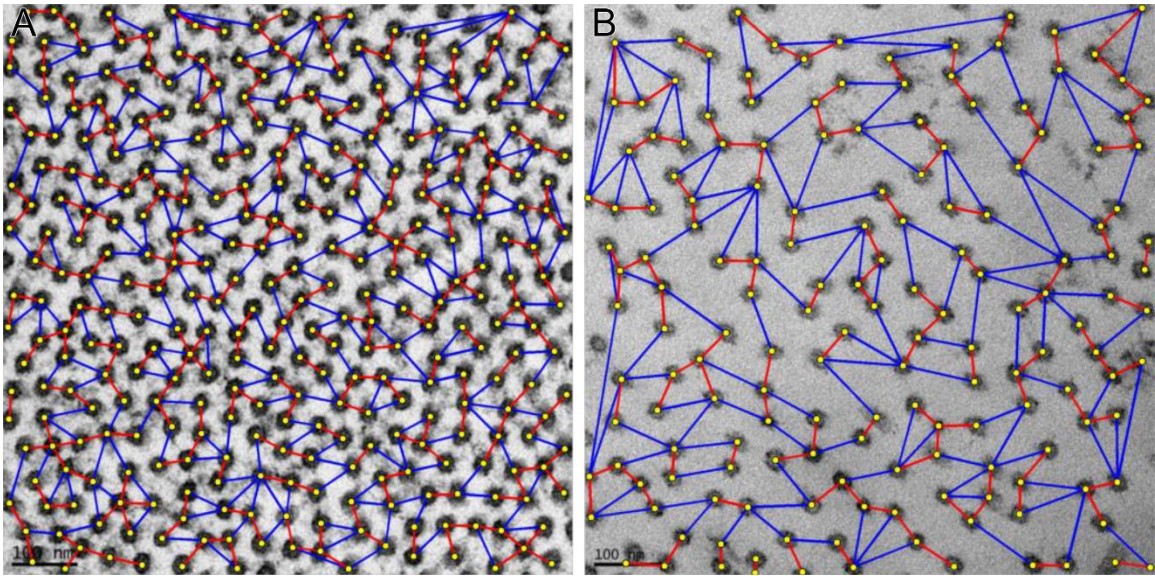


Figure 13. Representative transmission electron microscopy images of normal cornea (A) and alkali-burned (B) corneas, specifically measuring the minimum and maximum inter-fibrillar distances. Note the increased minimum (red) and maximum (blue) inter-fibrillar distances in the alkali-burned cornea compared to normal cornea.

APPENDIX 3: COPYRIGHT RELEASE

ELSEVIER LICENSE TERMS AND CONDITIONS

Nov 13, 2015

This is a License Agreement between Kristina Gronkiewicz ("You") and Elsevier ("Elsevier") provided by Copyright Clearance Center ("CCC"). The license consists of your order details, the terms and conditions provided by Elsevier, and the payment terms and conditions.

Supplier	Elsevier Limited The Boulevard, Langford Lane Kidlington, Oxford, OX5 1GB, UK
Registered Company Number	1982084
Customer name	Kristina Gronkiewicz
Customer address	900 East Campus Drive COLUMBIA, MO 65211
License number	3739440874013
License date	Oct 31, 2015
Licensed content publisher	Elsevier
Licensed content publication	Experimental Eye Research
Licensed content title	Development of a novel in vivo corneal fibrosis model in the dog
Licensed content author	K.M. Gronkiewicz, E.A. Giuliano, K. Kuroki, F. Bunyak, A. Sharma, L.B.C. Teixeira, C.W. Hamm, R.R. Mohan
Licensed content date	February 2016
Licensed content volume number	143
Licensed content issue number	n/a

Number of pages	14
Start Page	75
End Page	88
Type of Use	reuse in a thesis/dissertation
Portion	full article
Format	print
Are you the author of this Elsevier article?	Yes
Will you be translating?	No
Title of your thesis/dissertation	Therapeutic Potential of the Anti-Fibrotic Drug Suberanilohydroxamic Acid (SAHA) in Canine Corneal Fibrosis
Expected completion date	Jan 2016
Estimated size (number of pages)	75
Elsevier VAT number	GB 494 6272 12
Permissions price	0.00 USD
VAT/Local Sales Tax	0.00 USD / 0.00 GBP
Total	0.00 USD

BIBLIOGRAPHY

1. Labelle AL, Psutka K, Collins SP, et al. Use of hydropulsion for the treatment of superficial corneal foreign bodies: 15 cases (1999-2013). *J Am Vet Med Assoc* 2014;244:476-479.
2. Pumphrey SA, Pizzirani S, Pirie CG. 360-degree conjunctival grafting for management of diffuse keratomalacia in a dog. *Vet Ophthalmol* 2011;14:209-213.
3. Gray ME, West CE. Corneal injuries from liquid detergent pods. *J Aapos* 2014;18:494-495.
4. Guell JL, Verdaguer P, Elies D, et al. Persistent stromal scar after PRK and CXL: different preoperative findings, similar complication. *J Refract Surg* 2015;31:211-212.
5. Fini ME, Stramer BM. How the cornea heals: cornea-specific repair mechanisms affecting surgical outcomes. *Cornea* 2005;24:S2-s11.
6. Pascolini D, Mariotti SP. Global estimates of visual impairment: 2010. *Br J Ophthalmol* 2012;96:614-618.
7. Robaei D, Watson S. Corneal blindness: a global problem. *Clin Experiment Ophthalmol* 2014;42:213-214.
8. Netto MV, Mohan RR, Ambrosio R, Jr., et al. Wound healing in the cornea: a review of refractive surgery complications and new prospects for therapy. *Cornea* 2005;24:509-522.
9. Jester JV, Petroll WM, Cavanagh HD. Corneal stromal wound healing in refractive surgery: the role of myofibroblasts. *Prog Retin Eye Res* 1999;18:311-356.
10. Yamanaka O, Liu CY, Kao WW. Fibrosis in the anterior segments of the eye. *Endocr Metab Immune Disord Drug Targets* 2010;10:331-335.
11. Myrna KE, Pot SA, Murphy CJ. Meet the corneal myofibroblast: the role of myofibroblast transformation in corneal wound healing and pathology. *Vet Ophthalmol* 2009;12 Suppl 1:25-27.
12. Gordon GM, Ledee DR, Feuer WJ, et al. Cytokines and signaling pathways regulating matrix metalloproteinase-9 (MMP-9) expression in corneal epithelial cells. *J Cell Physiol* 2009;221:402-411.
13. Benito MJ, Calder V, Corrales RM, et al. Effect of TGF-beta on ocular surface epithelial cells. *Exp Eye Res* 2013;107:88-100.
14. Wilson SE. Corneal myofibroblast biology and pathobiology: generation, persistence, and transparency. *Exp Eye Res* 2012;99:78-88.
15. Maltseva O, Folger P, Zekaria D, et al. Fibroblast growth factor reversal of the corneal myofibroblast phenotype. *Invest Ophthalmol Vis Sci* 2001;42:2490-2495.
16. Netto MV, Mohan RR, Sinha S, et al. Stromal haze, myofibroblasts, and surface irregularity after PRK. *Exp Eye Res* 2006;82:788-797.
17. Zeisberg M, Kalluri R. Cellular mechanisms of tissue fibrosis. 1. Common and organ-specific mechanisms associated with tissue fibrosis. *Am J Physiol Cell Physiol* 2013;304:C216-225.
18. Saika S. TGF-beta signal transduction in corneal wound healing as a therapeutic target. *Cornea* 2004;23:S25-30.

19. Jester JV, Huang J, Barry-Lane PA, et al. Transforming growth factor(beta)-mediated corneal myofibroblast differentiation requires actin and fibronectin assembly. *Invest Ophthalmol Vis Sci* 1999;40:1959-1967.
20. Nishida K, Sotozono C, Adachi W, et al. Transforming growth factor-beta 1, -beta 2 and -beta 3 mRNA expression in human cornea. *Curr Eye Res* 1995;14:235-241.
21. Poniatowski LA, Wojdasiewicz P, Gasik R, et al. Transforming growth factor Beta family: insight into the role of growth factors in regulation of fracture healing biology and potential clinical applications. *Mediators Inflamm* 2015;2015:137823.
22. ten Dijke P, Geurts van Kessel AH, Foulkes JG, et al. Transforming growth factor type beta 3 maps to human chromosome 14, region q23-q24. *Oncogene* 1988;3:721-724.
23. Barton DE, Foellmer BE, Du J, et al. Chromosomal mapping of genes for transforming growth factors beta 2 and beta 3 in man and mouse: dispersion of TGF-beta gene family. *Oncogene Res* 1988;3:323-331.
24. Fujii D, Brissenden JE, Derynck R, et al. Transforming growth factor beta gene maps to human chromosome 19 long arm and to mouse chromosome 7. *Somat Cell Mol Genet* 1986;12:281-288.
25. Ashish Tandon¹ A, Jonathan C. K. Tovey^{1,2A}, Ajay Sharma^{1,2A}, Rangan Gupta^{1,2A}, and Rajiv R. Mohan^{1,2A,B,*}. Role of transforming growth factor beta in corneal function, biology and pathology. *Curr Mol Med* 2010;10:565-578.
26. Karamichos D, Guo XQ, Hutcheon AE, et al. Human corneal fibrosis: an in vitro model. *Invest Ophthalmol Vis Sci* 2010;51:1382-1388.
27. Carrington LM, Albon J, Anderson I, et al. Differential Regulation of Key Stages in Early Corneal Wound Healing by TGF- β Isoforms and Their Inhibitors. *Investigative Ophthalmology & Visual Science* 2006;47:1886-1894.
28. Jester JV, Barry-Lane PA, Cavanagh HD, et al. Induction of alpha-smooth muscle actin expression and myofibroblast transformation in cultured corneal keratocytes. *Cornea* 1996;15:505-516.
29. Huh MI, Kim YH, Park JH, et al. Distribution of TGF-beta isoforms and signaling intermediates in corneal fibrotic wound repair. *J Cell Biochem* 2009;108:476-488.
30. Lee JJ, Kim MK, Shin KS, et al. Transforming growth factor-beta expression in rat eyes with mechanical debridement of corneal epithelium or epithelial flap. *J Cataract Refract Surg* 2008;34:662-669.
31. Karamichos D, Hutcheon AE, Zieske JD. Transforming growth factor-beta3 regulates assembly of a non-fibrotic matrix in a 3D corneal model. *J Tissue Eng Regen Med* 2011;5:e228-238.
32. Akhurst RJ, Hata A. Targeting the TGFbeta signalling pathway in disease. *Nat Rev Drug Discov* 2012;11:790-811.
33. Tandon A, Tovey JC, Sharma A, et al. Role of transforming growth factor Beta in corneal function, biology and pathology. *Curr Mol Med* 2010;10:565-578.
34. Kume S, Haneda M, Kanasaki K, et al. SIRT1 inhibits transforming growth factor beta-induced apoptosis in glomerular mesangial cells via Smad7 deacetylation. *J Biol Chem* 2007;282:151-158.

35. LEASK A, ABRAHAM DJ. TGF- β signaling and the fibrotic response. *The FASEB Journal* 2004;18:816-827.
36. Joko T, Shiraishi A, Akune Y, et al. Involvement of P38MAPK in human corneal endothelial cell migration induced by TGF-beta(2). *Exp Eye Res* 2013;108:23-32.
37. Kretzschmar M, Doody J, Timokhina I, et al. A mechanism of repression of TGFbeta/ Smad signaling by oncogenic Ras. *Genes Dev* 1999;13:804-816.
38. Ollivier FJ, Gilger BC, Barrie KP, et al. Proteinases of the cornea and preclear tear film. *Vet Ophthalmol* 2007;10:199-206.
39. Sun YC, Hsiao CH, Chen WL, et al. Overexpression of matrix metalloproteinase-1 (MMP-1) and MMP-3 in superior limbic keratoconjunctivitis. *Invest Ophthalmol Vis Sci* 2011;52:3701-3705.
40. Kimura K, Orita T, Kondo Y, et al. Upregulation of matrix metalloproteinase expression by poly(I:C) in corneal fibroblasts: role of NF-kappaB and interleukin-1ss. *Invest Ophthalmol Vis Sci* 2010;51:5012-5018.
41. Kim YJ, Choi WI, Jeon BN, et al. Stereospecific effects of ginsenoside 20-Rg3 inhibits TGF-beta1-induced epithelial-mesenchymal transition and suppresses lung cancer migration, invasion and anoikis resistance. *Toxicology* 2014;322c:23-33.
42. Cheng S, Lovett DH. Gelatinase A (MMP-2) is necessary and sufficient for renal tubular cell epithelial-mesenchymal transformation. *Am J Pathol* 2003;162:1937-1949.
43. Islam SS, Mokhtari RB, El Hout Y, et al. TGF-beta1 induces EMT reprogramming of porcine bladder urothelial cells into collagen producing fibroblasts-like cells in a Smad2/Smad3-dependent manner. *J Cell Commun Signal* 2014;8:39-58.
44. Niu JY, Liu J, Liu L, et al. Construction of eukaryotic plasmid expressing human TGFBI and its influence on human corneal epithelial cells. *Int J Ophthalmol* 2012;5:38-44.
45. Kook H, Lepore JJ, Gitler AD, et al. Cardiac hypertrophy and histone deacetylase-dependent transcriptional repression mediated by the atypical homeodomain protein Hop. *J Clin Invest* 2003;112:863-871.
46. Kim N, Sun HY, Youn MY, et al. IL-1beta-specific recruitment of GCN5 histone acetyltransferase induces the release of PAF1 from chromatin for the de-repression of inflammatory response genes. *Nucleic Acids Res* 2013;41:4495-4506.
47. Suganuma T, Mushegian A, Swanson SK, et al. The ATAC acetyltransferase complex coordinates MAP kinases to regulate JNK target genes. *Cell* 2010;142:726-736.
48. Qian X, Chen J, Zhao D, et al. Plastrum testudinis induces gamma-globin gene expression through epigenetic histone modifications within the gamma-globin gene promoter via activation of the p38 MAPK signaling pathway. *Int J Mol Med* 2013;31:1418-1428.
49. Guo W, Shan B, Klingsberg RC, et al. Abrogation of TGF-beta1-induced fibroblast-myofibroblast differentiation by histone deacetylase inhibition. *Am J Physiol Lung Cell Mol Physiol* 2009;297:L864-870.
50. Van Wagoner DR, Nattel S. Insights into mechanisms linking cardiac hypertrophy and atrial fibrosis: evidence for a role of histone deacetylase in atrial fibrillation pathophysiology and therapy. *J Mol Cell Cardiol* 2008;45:707-708.

51. Zhou Q, Yang L, Wang Y, et al. TGF β mediated transition of corneal fibroblasts from a proinflammatory state to a profibrotic state through modulation of histone acetylation. *Journal of Cellular Physiology* 2010;224:135-143.
52. Sanders YY, Hagood JS, Liu H, et al. Histone deacetylase inhibition promotes fibroblast apoptosis and ameliorates pulmonary fibrosis in mice. *Eur Respir J* 2014;43:1448-1458.
53. Liu Y, Wang Z, Wang J, et al. A histone deacetylase inhibitor, largazole, decreases liver fibrosis and angiogenesis by inhibiting transforming growth factor-beta and vascular endothelial growth factor signalling. *Liver Int* 2013;33:504-515.
54. Liu N, He S, Ma L, et al. Blocking the class I histone deacetylase ameliorates renal fibrosis and inhibits renal fibroblast activation via modulating TGF-beta and EGFR signaling. *PLoS One* 2013;8:e54001.
55. Kinugasa F, Noto T, Matsuoka H, et al. Prevention of renal interstitial fibrosis via histone deacetylase inhibition in rats with unilateral ureteral obstruction. *Transpl Immunol* 2010;23:18-23.
56. Sharma A, Mehan MM, Sinha S, et al. Trichostatin a inhibits corneal haze in vitro and in vivo. *Invest Ophthalmol Vis Sci* 2009;50:2695-2701.
57. Donnelly KS, Giuliano EA, Sharma A, et al. Suberoylanilide hydroxamic acid (vorinostat): its role on equine corneal fibrosis and matrix metalloproteinase activity. *Veterinary Ophthalmology* 2014;17:61-68.
58. Bosniack AP, Giuliano EA, Gupta R, et al. Efficacy and safety of suberoylanilide hydroxamic acid (Vorinostat) in the treatment of canine corneal fibrosis. *Vet Ophthalmol* 2012;15:307-314.
59. Tandon A, Tovey JC, Waggoner MR, et al. Vorinostat: a potent agent to prevent and treat laser-induced corneal haze. *J Refract Surg* 2012;28:285-290.
60. Gu Y, Li X, He T, et al. The Antifibrosis Effects of Peroxisome Proliferator-Activated Receptor delta on Rat Corneal Wound Healing after Excimer Laser Keratectomy. *PPAR Res* 2014;2014:464935.
61. Milani BY, Milani FY, Park DW, et al. Rapamycin inhibits the production of myofibroblasts and reduces corneal scarring after photorefractive keratectomy. *Invest Ophthalmol Vis Sci* 2013;54:7424-7430.
62. Vezina M. Comparative Ocular Anatomy in Commonly Used Laboratory Animals In: Weir AaC, M, ed. *Assessing Ocular Toxicology in Laboratory Animals*: Springer, 2013;23-52.
63. Kern TJ. Ulcerative keratitis. *Vet Clin North Am Small Anim Pract* 1990;20:643-666.
64. Bentley E, Campbell S, Woo HM, et al. The effect of chronic corneal epithelial debridement on epithelial and stromal morphology in dogs. *Invest Ophthalmol Vis Sci* 2002;43:2136-2142.
65. Kadar T, Amir A, Cohen L, et al. Anti-VEGF Therapy (Bevacizumab) for Sulfur Mustard-Induced Corneal Neovascularization Associated with Delayed Limbal Stem Cell Deficiency in Rabbits. *Current Eye Research* 2013;39:439-450.
66. Berdahl JP, Johnson CS, Proia AD, et al. Comparison of sutures and dendritic polymer adhesives for corneal laceration repair in an in vivo chicken model. *Arch Ophthalmol* 2009;127:442-447.

67. Okada Y, Shirai K, Reinach PS, et al. TRPA1 is required for TGF-beta signaling and its loss blocks inflammatory fibrosis in mouse corneal stroma. *Lab Invest* 2014;94:1030-1041.
68. Bosiack AP, Giuliano EA, Gupta R, et al. Canine corneal fibroblast and myofibroblast transduction with AAV5. *Vet Ophthalmol* 2012;15:291-298.
69. Li X, Zhou Q, Hanus J, et al. Inhibition of multiple pathogenic pathways by histone deacetylase inhibitor SAHA in a corneal alkali-burn injury model. *Mol Pharm* 2013;10:307-318.
70. Ikeda Y, Ozono I, Tajima S, et al. Iron chelation by deferoxamine prevents renal interstitial fibrosis in mice with unilateral ureteral obstruction. *PLoS One* 2014;9:e89355.
71. Choi YJ, Kim DH, Kim SJ, et al. Decursin attenuates hepatic fibrogenesis through interrupting TGF-beta-mediated NAD(P)H oxidase activation and Smad signaling in vivo and in vitro. *Life Sci* 2014.
72. Chen Y, Yang S, Yao W, et al. Prostacyclin analogue beraprost inhibits cardiac fibroblast proliferation depending on prostacyclin receptor activation through a TGF beta-Smad signal pathway. *PLoS One* 2014;9:e98483.
73. Chen YL, Zhang X, Bai J, et al. Sorafenib ameliorates bleomycin-induced pulmonary fibrosis: potential roles in the inhibition of epithelial-mesenchymal transition and fibroblast activation. *Cell Death Dis* 2013;4:e665.
74. Rodier J, Sharma A, Tandon A, et al. RNAi Gene Silencing Of TGF-beta Signaling: A Powerful Approach To Control Corneal Fibrosis. *Invest Ophthalmol Vis Sci* 2013;54:5241-.
75. Das D, Holmes A, Murphy GA, et al. TGF-beta1-Induced MAPK activation promotes collagen synthesis, nodule formation, redox stress and cellular senescence in porcine aortic valve interstitial cells. *J Heart Valve Dis* 2013;22:621-630.
76. Nakagawa T, Lan HY, Glushakova O, et al. Role of ERK1/2 and p38 mitogen-activated protein kinases in the regulation of thrombospondin-1 by TGF-beta1 in rat proximal tubular cells and mouse fibroblasts. *J Am Soc Nephrol* 2005;16:899-904.
77. Yang Y, Wang Z, Yang H, et al. TRPV1 potentiates TGFbeta-induction of corneal myofibroblast development through an oxidative stress-mediated p38-SMAD2 signaling loop. *PLoS One* 2013;8:e77300.
78. Kim HS, Luo L, Pflugfelder SC, et al. Doxycycline inhibits TGF-beta1-induced MMP-9 via Smad and MAPK pathways in human corneal epithelial cells. *Invest Ophthalmol Vis Sci* 2005;46:840-848.
79. Choo QY, Ho PC, Tanaka Y, et al. The histone deacetylase inhibitors MS-275 and SAHA suppress the p38 mitogen-activated protein kinase signaling pathway and chemotaxis in rheumatoid arthritic synovial fibroblastic E11 cells. *Molecules* 2013;18:14085-14095.
80. Bruzzese F, Pucci B, Milone MR, et al. Panobinostat synergizes with zoledronic acid in prostate cancer and multiple myeloma models by increasing ROS and modulating mevalonate and p38-MAPK pathways. *Cell Death Dis* 2013;4:e878.
81. Chen X, Xiao W, Chen W, et al. The epigenetic modifier trichostatin A, a histone deacetylase inhibitor, suppresses proliferation and epithelial-mesenchymal transition of lens epithelial cells. *Cell Death Dis* 2013;4:e884.

82. Kim HS, Shang T, Chen Z, et al. TGF-beta1 stimulates production of gelatinase (MMP-9), collagenases (MMP-1, -13) and stromelysins (MMP-3, -10, -11) by human corneal epithelial cells. *Exp Eye Res* 2004;79:263-274.
83. Parkin BT, Smith VA, Easty DL. The control of matrix metalloproteinase-2 expression in normal and keratoconic corneal keratocyte cultures. *Eur J Ophthalmol* 2000;10:276-285.
84. Wang Z, Chen C, Finger SN, et al. Suberoylanilide hydroxamic acid: a potential epigenetic therapeutic agent for lung fibrosis? *Eur Respir J* 2009;34:145-155.
85. Culley KL, Hui W, Barter MJ, et al. Class I histone deacetylase inhibition modulates metalloproteinase expression and blocks cytokine-induced cartilage degradation. *Arthritis Rheum* 2013;65:1822-1830.
86. Ahmed S, Riegsecker S, Beamer M, et al. Largazole, a class I histone deacetylase inhibitor, enhances TNF- α -induced ICAM-1 and VCAM-1 expression in rheumatoid arthritis synovial fibroblasts. *Toxicology and Applied Pharmacology* 2013;270:87-96.
87. Marquez-Curtis LA, Qiu Y, Xu A, et al. Migration, proliferation, and differentiation of cord blood mesenchymal stromal cells treated with histone deacetylase inhibitor valproic acid. *Stem Cells International* 2014;2014.
88. Whittaker LRaP. Collagen and picrosirius red staining: a polarized light assessment of fibrillar hue and spatial distribution. *Braz J morphol Sci* 2005;22:97-104.
89. Junqueira LC, Cossermelli W, Brentani R. Differential staining of collagens type I, II and III by Sirius Red and polarization microscopy. *Arch Histol Jpn* 1978;41:267-274.
90. Sato T. A modified method for lead staining of thin sections. *Journal of Electron Microscopy* 1968;17:158-159.
91. Sun M, Huang J, Bunyak F, et al. Superresolution microscope image reconstruction by spatiotemporal object decomposition and association: application in resolving t-tubule structure in skeletal muscle. *Opt Express* 2014;22:12160-12176.
92. Ersoy I, Bunyak F, Higgins JM, et al. Coupled edge profile active contours for red blood cell flow analysis. Biomedical Imaging (ISBI), 2012 9th IEEE International Symposium on 2012;748-751.
93. Vincent L, Soille P. Watersheds in digital spaces: an efficient algorithm based on immersion simulations. *Pattern Analysis and Machine Intelligence, IEEE Transactions on* 1991;13:583-598.
94. Soille P. Morphological Image Analysis: Principles and Applications: Springer-Verlag Telos, 1999;170-171.
95. Nath S, Palaniappan K, Bunyak F. Cell Segmentation Using Coupled Level Sets and Graph-Vertex Coloring In: Larsen R, Nielsen M, Sporring J, eds. *Medical Image Computing and Computer-Assisted Intervention – MICCAI 2006*: Springer Berlin Heidelberg, 2006;101-108.
96. Salouti R, Nowroozzadeh MH, Zamani M, et al. Comparison of Horizontal corneal diameter measurements using the Orbscan IIz and Pentacam HR systems. *Cornea* 2013;32:1460-1464.
97. Henriksson JT, McDermott AM, Bergmanson JPG. Dimensions and Morphology of the Cornea in Three Strains of Mice. *Investigative ophthalmology & visual science* 2009;50:3648-3654.

98. Gimeno FL, Lavigne V, Gatto S, et al. Advances in corneal stem-cell transplantation in rabbits with severe ocular alkali burns. *Journal of Cataract and Refractive Surgery* 2007;33:1958-1965.
99. Puangrichareern V, Tseng SCG. Cytologic evidence of corneal diseases with limbal stem cell deficiency. *Ophthalmology* 1995;102:1476-1485.
100. Tseng SCG. Concept and application of limbal stem cells. *Eye* 1989;3:141-157.
101. Fatima A, Iftexhar G, Sangwan VS, et al. Ocular surface changes in limbal stem cell deficiency caused by chemical injury: A histologic study of excised pannus from recipients of cultured corneal epithelium. *Eye* 2008;22:1161-1167.
102. Huang AJ, Tseng SC. Corneal epithelial wound healing in the absence of limbal epithelium. *Invest Ophthalmol Vis Sci* 1991;32:96-105.
103. Gu HW, Hu N. Study on the establishment of corneal alkali chemical injury on rats. *International Eye Science* 2013;13:1093-1095.
104. Bentley E, Abrams GA, Covitz D, et al. Morphology and immunohistochemistry of spontaneous chronic corneal epithelial defects (SCCED) in dogs. *Invest Ophthalmol Vis Sci* 2001;42:2262-2269.
105. Stramer BM, Zieske JD, Jung JC, et al. Molecular mechanisms controlling the fibrotic repair phenotype in cornea: implications for surgical outcomes. *Invest Ophthalmol Vis Sci* 2003;44:4237-4246.
106. Denis HM. Anterior lens capsule disruption and suspected malignant glaucoma in a dog. *Vet Ophthalmol* 2002;5:79-83.
107. Graham JS, Schoneboom BA. Historical perspective on effects and treatment of sulfur mustard injuries. *Chem Biol Interact* 2013;206:512-522.
108. Buss DG, Giuliano EA, Sharma A, et al. Isolation and cultivation of equine corneal keratocytes, fibroblasts and myofibroblasts. *Vet Ophthalmol* 2010;13:37-42.
109. Dua HS. The conjunctiva in corneal epithelial wound healing. *British Journal of Ophthalmology* 1998;82:1407-1411.
110. Shapiro MS, Friend J, Thoft RA. Corneal re-epithelialization from the conjunctiva. *Investigative Ophthalmology and Visual Science* 1981;21:135-142.
111. Takahashi T, Cho HI, Kublin CL, et al. Keratan sulfate and dermatan sulfate proteoglycans associate with type VI collagen in fetal rabbit cornea. *Journal of Histochemistry and Cytochemistry* 1993;41:1447-1457.
112. Herwig MC, Müller AM, Holz FG, et al. Immunolocalization of different collagens in the cornea of human fetal eyes: A developmental approach. *Current Eye Research* 2013;38:60-69.
113. Sun M, Chen S, Adams SM, et al. Collagen V is a dominant regulator of collagen fibrillogenesis: Dysfunctional regulation of structure and function in a corneal-stroma-specific Col5a1-null mouse model. *Journal of Cell Science* 2011;124:4096-4105.
114. Doane KJ, Yang G, Birk DE. Corneal cell-matrix interactions: Type VI Collagen promotes adhesion and spreading of corneal fibroblasts. *Experimental Cell Research* 1992;200:490-499.
115. Hassell JR, Birk DE. The molecular basis of corneal transparency. *Experimental Eye Research* 2010;91:326-335.

116. Xie SB, Yao JL, Zheng SS, et al. The levels of serum fibrosis marks and morphometric quantitative measurement of hepatic fibrosis. *Hepatobiliary and Pancreatic Diseases International* 2002;1:202-206.
117. Chen S, Puthanveetil P, Feng B, et al. Cardiac miR-133a overexpression prevents early cardiac fibrosis in diabetes. *Journal of Cellular and Molecular Medicine* 2014;18:415-421.
118. Abo-Zenah H, Katsoudas S, Wild G, et al. Early human renal allograft fibrosis: Cellular mediators. *Nephron* 2002;91:112-119.
119. Ding H, Ma JJ, Wang WP, et al. Assessment of liver fibrosis: The relationship between point shear wave elastography and quantitative histological analysis. *Journal of Gastroenterology and Hepatology (Australia)* 2015;30:553-558.
120. Sanyal AJ, Contos MJ, Yager D, et al. Development of pseudointima and stenosis after transjugular intrahepatic portosystemic shunts: Characterization of cell phenotype and function. *Hepatology* 1998;28:22-32.
121. Janin-Manificat H, Rovere MR, Galiacy SD, et al. Development of ex vivo organ culture models to mimic human corneal scarring. *Mol Vis* 2012;18:2896-2908.
122. Lee YC, Wang IJ, Hu FR, et al. Immunohistochemical study of subepithelial haze after phototherapeutic keratectomy. *J Refract Surg* 2001;17:334-341.
123. Carrington SD, Alexander RA, Grierson I. Elastic and related fibres in the normal cornea and limbus of the domestic cat. *Journal of Anatomy* 1984;139:319-332.
124. Kamma-Lorger CS, Boote C, Hayes S, et al. Collagen and mature elastic fibre organisation as a function of depth in the human cornea and limbus. *J Struct Biol* 2010;169:424-430.
125. Donovan RH, Carpenter RL, Schepens CL, et al. Histology of the normal collie eye: I. Topography, cornea, sclera and filtration angle. *Ann Ophthalmol* 1974;6:257-260 passim.
126. Enomoto N, Suda T, Kono M, et al. Amount of elastic fibers predicts prognosis of idiopathic pulmonary fibrosis. *Respir Med* 2013;107:1608-1616.
127. Thomas BJ, Galor A, Nanji AA, et al. Ultra high-resolution anterior segment optical coherence tomography in the diagnosis and management of ocular surface squamous neoplasia. *Ocul Surf* 2014;12:46-58.
128. El Sanharawi M, Sandali O, Basli E, et al. Fourier-Domain Optical Coherence Tomography Imaging in Corneal Epithelial Basement Membrane Dystrophy: A Structural Analysis. *Am J Ophthalmol* 2015.
129. Bouheraoua N, Jouve L, El Sanharawi M, et al. Optical coherence tomography and confocal microscopy following three different protocols of corneal collagen-crosslinking in keratoconus. *Invest Ophthalmol Vis Sci* 2014;55:7601-7609.
130. Chan JB, Yuen LH, Huang EH, et al. Reproducibility of cornea measurements in anterior segment OCT images of normal eyes and eyes with bullous keratopathy analyzed with the Zhongshan Assessment Program. *Invest Ophthalmol Vis Sci* 2011;52:8884-8890.
131. Rush SW, Han DY, Rush RB. Optical coherence tomography-guided transepithelial phototherapeutic keratectomy for the treatment of anterior corneal scarring. *Am J Ophthalmol* 2013;156:1088-1094.

132. Akhtar S. Effect of processing methods for transmission electron microscopy on corneal collagen fibrils diameter and spacing. *Microscopy Research and Technique* 2012;75:1420-1424.
133. Akhtar S, Alkatan H, Kirat O, et al. Ultrastructural and three-dimensional study of post-LASIK ectasia cornea. *Microscopy Research and Technique* 2014;77:91-98.
134. Komai Y, Ushiki T. The three-dimensional organization of collagen fibrils in the human cornea and sclera. *Investigative Ophthalmology and Visual Science* 1991;32:2244-2258.
135. Nagayasu A, Hosaka Y, Yamasaki A, et al. A preliminary study of direct application of atelocollagen into a wound lesion in the dog cornea. *Curr Eye Res* 2008;33:727-735.
136. Kafarnik C, Fritsche J, Reese S. Corneal innervation in mesocephalic and brachycephalic dogs and cats: assessment using in vivo confocal microscopy. *Vet Ophthalmol* 2008;11:363-367.
137. McCally RL, Freund DE, Zorn A, et al. Light-scattering and ultrastructure of healed penetrating corneal wounds. *Invest Ophthalmol Vis Sci* 2007;48:157-165.
138. Dawson DG, Kramer TR, Grossniklaus HE, et al. Histologic, ultrastructural, and immunofluorescent evaluation of human laser-assisted in situ keratomileusis corneal wounds. *Arch Ophthalmol* 2005;123:741-756.
139. Gray LL, Hillier A, Cole LK, et al. The effect of ketoconazole on whole blood and skin ciclosporin concentrations in dogs. *Vet Dermatol* 2013;24:118-125 e127-118.
140. Naughton JF, Stewart MC, Ciobanu L, et al. Contrast magnetic resonance imaging for measurement of cartilage glycosaminoglycan content in dogs: a pilot study. *Vet Comp Orthop Traumatol* 2013;26:100-104.
141. Dupre G, Coudek K. Laparoscopic-assisted placement of a peritoneal dialysis catheter with partial omentectomy and omentopexy in dogs: an experimental study. *Vet Surg* 2013;42:579-585.
142. Frangi A, Niessen W, Vincken K, et al. Multiscale vessel enhancement filtering In: Wells W, Colchester A, Delp S, eds. *Medical Image Computing and Computer-Assisted Intervention — MICCAI'98*: Springer Berlin Heidelberg, 1998;130-137.

VITA

On August 15, 1986, Kristina Marie Gronkiewicz was born in Chicago, Illinois. Following her high school education at Benet Academy in Lisle, Illinois, Kristina enrolled as an undergraduate student at Emory University in Atlanta, Georgia. Here, she earned a Bachelor of Science with majors in Biology and English in 2008. Upon completion of undergraduate, Kristina entered the College of Veterinary Medicine at University of Illinois and received her Doctorate in Veterinary Medicine (DVM) in 2012. After earning her DVM, Kristina completed a one year small animal medicine and surgery rotating internship at Oklahoma State University. Kristina entered her 3 year Comparative Ophthalmology Residency and Masters of Biomedical Science programs at the University of Missouri in 2013.